Effects of Rotation on the Multi-Scale Organization of Convection in a Global 2-D Cloud-Resolving Model

Qiu Yang*

Center for Prototype Climate Modeling, New York University Abu Dhabi, Saadiyat Island, Abu Dhabi, UAE

Andrew J. Majda

Department of Mathematics and Center for Atmosphere Ocean Science, Courant Institute of Mathematical Sciences, New York University, New York, NY, USA,

Center for Prototype Climate Modeling, New York University Abu Dhabi, Saadiyat Island, Abu Dhabi, UAE

Noah D. Brenowitz

Department of Atmospheric Sciences, University of Washington, Seattle, WA, USA

**Corresponding author address:* Qiu Yang, Courant Institute of Mathematical Sciences, New York University, 251 Mercer Street, New York, NY, 10012

E-mail: yangq@cims.nyu.edu

ABSTRACT

Atmospheric convection exhibits distinct spatio-temporal variability at different latitudes. A good understanding of the effects of rotation on the multi-scale organization of convection from mesoscale to synoptic scale to planetary scale is still lacking. Here cloud-resolving simulations with fixed surface fluxes and radiative cooling are implemented with constant rotation in a two-dimensional (2-D) planetary domain to simulate multi-scale organization of convection from the tropics to mid-latitudes. All scenarios are divided into three rotation regimes (weak, order-one, and strong) to represent idealized ITCZ region ($0^\circ \sim 6^\circ$ N), Indian monsoon region ($6^\circ \sim 20^\circ$ N), and mid-latitude region ($20^\circ \sim 45^\circ$ N), respectively. In each rotation regime, a multi-scale asymptotic model is derived systematically and used as a diagnostic framework for energy budget analysis. The results show that planetary-scale organization of convection only arises in the weak rotation regime, while synoptic-scale organization dominates (vanishes) in the order-one (strong) rotation regime. The depletion of planetary-scale organization of convection as the magnitude of rotation increases is attributed to the reduced planetary kinetic energy of zonal winds, mainly due to the decreasing acceleration effect by eddy zonal momentum transfer from mesoscale convective systems (MCSs) and increasing deceleration effect by the Coriolis force. Similarly, the maintenance of synoptic-scale organization is related to the acceleration effect by MCSs. Such decreasing acceleration effects by MCSs on both planetary and synoptic scales are further attributed to less favorable conditions for convection provided by background sounding of low-level equivalent potential temperature and vertical shear of zonal winds, resulting from the increasing magnitude of rotation.

1. Introduction

Atmospheric convection plays a crucial role in the horizontal and vertical transport of momentum, heat, and moisture of large-scale circulation on the earth (Schneider 2006). After decades of observational studies based on satellite and in situ measurements, it is apparent now that the spatio-temporal variability of convection has distinct characteristics at different latitudes (Riemann-Campe et al. 2009). Specifically, tropical convection is organized in a hierarchy of spatio-temporal scales, ranging from a cumulus cloud of several kilometers and a few minutes to MCSs (Houze 2004) of several hundred kilometers and a few hours to convective coupled equatorial waves (CCEWs) (Kiladis et al. 2009) of thousand kilometers and 1-2 weeks to the Madden-Julian oscillations (MJOs) (Zhang 2005) of ten thousand kilometers and 1-3 months. In contrast, convection in the subtropics is dominated by synoptic-scale convective disturbances such as low pressure systems in the Indian monsoon trough region (Hurley and Boos 2015). Theoretically, the magnitude of rotation can dramatically influence the behavior of geophysical flows (Majda 2000). In the mid-latitudes, the strong rotation leads to a strict temporal frequency scale separation between potential vorticity dynamics and fast gravity waves. In contrast, the weak rotation in the tropics does not induce a time scale separation any more but allows multi-scale organization of convection in the presence of warm surface temperature and abundant moisture (Majda 2012).

Contemporary global climate models (GCMs) struggle to accurately simulate the multi-scale organization of tropical convection. In fact, present-day GCMs still have difficulty in simulating key features of propagating MJOs (Jiang et al. 2015), although predictions of the MJO have improved over the past decade (Kim et al. 2018). Furthermore, it is observed that the MJO is a slowly eastward-moving planetary-scale envelope that contains a few superclusters of cloudiness with numerous embedded cloud clusters (Nakazawa 1988; Chen et al. 1996). Even good GCMs fail to satisfyingly simulate these multi-scale features (Guo et al. 2015). It is hypothesized here that the poorly simulated MJOs in the GCMs is due to an inadequate treatment of multi-scale interactions of convection, especially the upscale impact of organized tropical convection such as MCSs that are poorly resolved in the coarse-resolution GCM simulations.

To address this issue, it is necessary to obtain a better understanding of spatio-temporal scale selection and multi-scale interactions of convection. With the development of computational resource, cloud-resolving models (CRMs) have become a practically useful tool for simulating organized convection in a fine horizontal resolution of a few kilometers (Khairoutdinov and Randall 2003; Miura et al. 2007; Tao and Moncrieff 2009; Guichard and Couvreux 2017). In particular, the 2-D CRM simulations provide a cheap way to study the multi-scale organization of convection in a planetary domain. For example, the idealized 2-D CRM simulation by Grabowski and Moncrieff (2001) showed that convection in background easterly winds is organized in a two-scale structure with a synoptic-scale envelope moving eastward and numerous embedded MCSs moving westward. Slawinska et al. (2014) showed that the Walker circulation over a warm pool exhibits intraseasonal variability with outward (inward) moving synoptic-scale systems during its expansion (contraction) phases. Due to expensive computational cost, many three-dimensional (3-D) CRM simulations only focused on radiative convective equilibrium in small domains (Held et al. 1993; Bretherton et al. 2005). In the absence of rotation, those disordered and scattered small-scale clouds arising from initial disturbances in a moist unstable environment coalesce into large-scale patches of convection, which is known as self-aggregation (Bretherton et al. 2005; Muller and Held 2012; Wing and Emanuel 2014). Bretherton et al. (2005) recognized the self-aggregation as an instability driven by convection-water vapor-radiation-surface fluxes feedbacks. However, those theories for explaining large-scale organization of convection mostly focus on thermodynamic effects, while dynamic effects due to multi-scale interactions are overlooked. Moreover, the absence of rotation makes the model setup less realistic.

In fact, several studies have been conducted to investigate the effects of rotation on scale selection and multi-scale organization of convection. Majda et al. (2015) used the multicloud model (Khouider and Majda 2006c,a,b, 2007) with either a deterministic (Khouider and Majda 2008b,a) or stochastic (Khouider et al. 2010; Deng et al. 2015; Goswami et al. 2017) convective heating closure to simulate organized convection in a rotating 2-D flow. They concluded that the planetary rotation is one of important players in the diminishing of organized convection and convectively coupled gravity wave activity, and deep convection activity in the stochastic model simulations becomes patchy and unorganized in the subtropics and mid-latitudes. The 2-D nonhydrostatic anelastic model simulation by Liu and Moncrieff (2004) indicated that rotation-induced localized descent stabilizes and dries the neighborhood of convective region, explaining the fact that the tropics is a preferred region for convective clustering. In general, planetary rotation has significant impact on background sounding of thermodynamic fields and vertical shear, the latter of which plays a crucial role in promoting organized convection (Newton and Rodebush Newton 1959; Moncrieff 1981; Moncrieff and Liu 1999; Tompkins 2001).

The goals of this paper include the following four aspects, 1) using a global 2-D CRM to simulate multi-scale organization of convection in three regimes with weak, order-one, and strong rotation, respectively; 2) deriving a multi-scale asymptotic model for upscale and downscale impacts in each rotation regime and using it as a diagnostic framework for energy budget analysis; 3) explaining why planetary-scale organization diminishes in the weak rotation regime as the magnitude of rotation increases and investigating the role of eddy transfer of momentum, temperature, and equivalent potential temperature from meso- and synoptic-scale fluctuations; 4) explaining why synoptic-scale organization persists in the order-one rotation regime but diminishes in the strong rotation regime.

Here we use the System for Atmospheric Modeling (SAM) (Khairoutdinov and Randall 2003) to investigate the effects of rotation on the multi-scale organization of convection. Thanks to its easy configuration and fast execution, the SAM model has been used widely to simulate large-scale organization of convection in idealized domain geometry (Bretherton et al. 2005; Wing and Emanuel 2014; Bretherton and Khairoutdinov 2015; Wing and Cronin 2016). In particular, Brenowitz et al. (2018) configured the model in a global 2-D periodic domain to simulate organized convection without the rotation. With both radiative cooling and surface fluxes fixed, the simulation in background easterly winds still produces an eastward-moving planetary-scale envelope of convection with multiple superclusters of cloudiness and numerous embedded clusters. To identify physical mechanisms behind the multi-scale organization, Brenowitz et al. (2018) decomposed the model outputs into meso-, synoptic-, and planetary-scale components and concluded the key role of multi-scale interactions in promoting large-scale organization of convection based on energy budget analysis. Here we configure the SAM model in a similar way as Brenowitz et al. (2018) but with the Coriolis force. The magnitude of rotation is varied to represent three different regimes, including the ITCZ regime with weak rotation, the Indian monsoon trough regime with order-one rotation, and the mid-latitude regime with strong rotation.

In each regime, we derive a multi-scale model by following the multi-scale asymptotic methods (Majda and Klein 2003; Majda 2007) and use it as a diagnostic framework for energy budget analysis. In particular, the multi-scale models in the weak and order-one rotation regimes are derived under the standard physical scaling in the tropics (Majda 2007). Consequently, the governing equations across synoptic- and meso-scales are similar to the mesoscale equatorial synoptic dynamics (MESD) model (Majda 2007), and those across planetary- and synoptic-scales resemble the intraseasonal multi-scale moist dynamics (IMMD) model (Biello and Majda 2010; Back and Biello 2018). Notably, the MESD model has been used to study the upscale impact of MCSs on convectively coupled Kelvin waves (CCKWs) (Yang and Majda 2017, 2018) and 2-day waves (Yang and Majda 2019). In contrast, the multi-scale model in the strong rotation regime follows the classic quasi-geostrophic (QG) scaling (Vallis 2017).

We run 10 SAM model simulations under the similar configuration as Brenowitz et al. (2018) but with increasing magnitude of rotation. Several key results about the effects of rotation are obtained. First of all, planetary-scale organization of convection only arises in the weak rotation regime, while synoptic-scale organization persists in the order-order rotation regime but diminishes as the magnitude of rotation further increases. As summarized by the schematic diagram in Fig. 9, the diminishment of planetary-scale organization is attributed to two changing effects in terms of planetary kinetic energy budget of zonal winds, including decreasing acceleration effect by eddy zonal momentum transfer from mesoscale fluctuations and increasing deceleration effect by the Coriolis force. As for the acceleration effect from upscale impact of MCSs, its decreasing strength is attributed to less favorable conditions for convection provided by background sounding of both low-level equivalent potential temperature and vertical shear of zonal winds, resulting from the increasing magnitude of rotation. Similarly, the maintenance of synoptic-scale organization in the order-one rotation regime and its diminishment in strong rotation regime is also related to the decreasing acceleration effect from upscale impact of MCSs, as summarized by the schematic diagram in Fig.15.

The rest of the paper is organized as follows. Section 2 describes the model configuration and experiment design. Section 3 shows the spatio-temporal variability of brightness temperature and the zonal-mean climatology of winds and thermodynamic fields with different magnitude of rotation. A multi-scale decomposition method is introduced to decompose total fields into domain-mean and planetary-, synoptic-, meso-scale fluctuations. Section 4 investigates the planetary-scale kinetic energy budget of zonal and meridional winds and available potential energy in the weak rotation regime, and highlights the key role of eddy transfer of momentum, temperature, and equivalent potential temperature. Section 5 does a similar energy budget analysis for synoptic-scale flow fields in the order-one rotation regime, while Section 6 considers the strong rotation regime. The paper concludes with a discussion in Section 7.

2. Model Configuration and Experiment Design

The SAM model version 6.11.1 is used here under the similar configuration as the QSTRAT simulation in Brenowitz et al. (2018) but with the Coriolis force. All simulations use the single-moment microphysics and the CAM3 radiation packages, Smolarkiewicz's MPDATA advection scheme with monotonic corrector, and the 1.5-order closure (prognostic SGS turbulent kinetic energy) subgrid-scale scheme. In order to exclude effects of surface fluxes, we perform all simulations over a uniform 300.15 K sea surface temperature (SST) ocean surface with latent and sensible heat fluxes fixed at 210.6 Wm^{-2} and 31.20 Wm^{-2}, respectively. To avoid effects of active radiation, we prescribe a fixed radiative cooling of 1.5 $Kday^{-1}$ below 150 hPa and a constant stratospheric heating of 4.5 $Kday^{-1}$ above. The stratospheric heating increases stratification of the atmosphere near the tropopause, turning the troposphere into a rigid-lid scenario. Similar to Grabowski and Moncrieff (2001), the zonal winds are nudging towards -10 ms^{-1} easterly background winds with nudging time scale 1 day. A sponge layer is added at the domain top to damp gravity waves. The 2-D planetary domain has $2^{15} = 32768$ km zonal extent in a 2 km horizontal resolution and 27 km vertical extent with 64 vertical levels. All simulations are run for 100 days, and the last 80-day solutions are used for diagnostic analysis.

Here we repeat the non-rotating simulation in Brenowitz et al. (2018) as the control experiment and run another 9 simulations with increasing magnitude of rotation from the tropics to the mid-latitude in the Northern Hemisphere (NH). The counterparts in the Southern Hemisphere can be induced based on the mirror symmetry about the equator. It is worth mentioning that the standard synoptic time scale is about 8 hrs (Majda 2007), equivalent to the reciprocal of Coriolis frequency f at the latitude 14 deg N. As shown by Table 1, we divide all rotating scenarios into three regimes, including i) the ITCZ regime with weak rotation ($0 \sim 6^\circ$ N), ii) the Indian monsoon trough regime with order-one rotation ($6^\circ \sim 20^\circ$ N), and iii) the mid-latitude regime with strong rotation ($> 20^\circ$ N). We choose these three rotation regimes, not only because of the observation that convection exhibits distinct characteristics in the tropics, subtropics, and mid-latitudes, but also the different properties of governing equations as shown in Table 2-4. Besides, the second regime is referred to as the order-one rotation regime, because the corresponding Coriolis frequency is comparable to its standard value at the latitude 14 deg N.

3. Effects of Rotation on the Multi-scale Organization of Convection

In this section, we first study the spatio-temporal variability of brightness temperature and 850-hPa zonal winds, which represent thermodynamic and dynamic aspects of convection, respectively. Notably, Fig.1 and Fig.2 show that planetary-scale organization of convection only arises in the weak rotation regime, while synoptic-scale organization persists in the order-one rotation regime but diminishes in the strong rotation regime. The effects of rotation on zonal-mean climatology of flow fields are also investigated.

a. Spatio-temporal variability of brightness temperature and 850-hPa zonal winds

Fig. 1a shows the Hovmöller diagram of brightness temperature in the non-rotating case, which is the same as Brenowitz et al. (2018). In the first 5 days, numerous westward-moving MCSs are organized into a few eastward-moving synoptic-scale envelopes. After that, a planetary-scale envelope of convection at wavenumber 2 gradually forms and propagates eastward at a speed of 7 m/s. This planetary-scale envelope contains several eastward-moving synoptic-scale disturbances in the leading edge and westward-moving disturbances in the trailing edge with numerous embedded westward-moving MCSs. Fig. 1b-h are for the remaining 7 cases (last 2 cases in the strong rotation regime are not shown). In the weak rotation regime, the planetary-scale organization of convection arises at the latitude 1° N in panel (b) but diminishes in panels (c) and (d). In contrast, panels (e-g) show that synoptic-scale envelopes with embedded westward-moving MCSs dominate in the order-one rotation regime, resembling the two-scale organization of convection in Grabowski and Moncrieff (2001). As the magnitude of rotation increases, the length scale of synoptic-scale envelopes becomes smaller, while their propagation speed is faster. At the latitude 27° N in panel (h) in the strong rotation regime, scattered MCSs prevail over the whole domain, which is akin to the mid-latitude case in Liu and Moncrieff (2004).

Fig. 2a shows the wavenumber-frequency spectra of brightness temperature in the non-rotating case. The spectra of brightness temperature is dominated by a peak at wavenumber 2 and period of 26.7 days, which further extends to larger wavenumber and shorter period along a straight line across the origin. In contrast, the spectra of westward-moving modes is much weaker. Fig. 2b shows the spectra of 850-hPa zonal velocity, which is similar to panel (a) but with the significant spectra of westward-moving modes at wavenumber 1-5. Fig. 2c-r are for the remaining 8 cases (last case in the strong rotation regime is not shown). Panels (c) and (d) at the latitude 1° N resemble panels (a) and (b). As the magnitude of rotation increases in the weak rotation regime, the spectra accounting for eastward-moving envelopes gradually shifts to smaller spatial and temporal scales in panels (e-j). It is worth mentioning that the period of eastward-moving envelopes are longer than the corresponding time scale of the Coriolis force. Panels (k-r) show the spectra in the order-one and strong rotation regimes. Overall, the maximum strength of spectra decays gradually as the magnitude of rotation increases, indicating the diminishing spatio-temporal variability of convection. Besides, the spectra band of westward-moving modes shifts along with the peak of eastward-moving envelopes, reflecting the modulation effect by the latter.

b. Zonal-mean climatology of winds, moisture, and (equivalent) potential temperature

Fig. 3 shows the zonal-mean climatology of zonal and meridional velocity, density, water vapor, and (equivalent) potential temperature. As shown by panel (a), zonal winds in the non-rotating case feature significant anomalies from -10 ms^{-1} background easterly winds throughout the troposphere, including weak winds below 950 hPa due to boundary layer (BL) friction and easterly (westerly) anomalies in the lower (upper) troposphere. The vertical shear in the free troposphere diminishes gradually as the magnitude of rotation increases, while that in the BL keeps unchanged. In contrast, the presence of the Coriolis force induces significant meridional winds in panel (b) with northerlies below 950 hPa, southerlies between 950 hPa and 600 hPa, and northerlies above 400 hPa. Vertical profiles of density, potential temperature are mostly similar among all cases in panels (c) and (d). As shown by panel (e), water vapor decreases exponentially in height with most of water vapor contained below 600 hPa. Equivalent potential temperature in panel (f) is characterized by negative vertical gradient below 700 hPa and positive vertical gradient above that level. As the magnitude of rotation increases, the lower and middle troposphere become more moist near 700 hPa with larger value of moisture and equivalent potential temperature. The resulting reduced vertical gradient of equivalent potential temperature in the lower troposphere provides less favorable conditions for convection.

c. Multi-scale decomposition of flow fields across planetary-, synoptic- and meso-scales

In order to facilitate diagnostic analysis for multi-scale interactions in the following sections, we introduce a multi-scale decomposition method based on the coarse-graining technique, a straightforward generalization of asymptotic averaging operators (Majda 2007) in a finite domain with small grid spacing. The detailed procedure for decomposing total fields into domain mean, and planetary-, synoptic-, meso-scale fluctuations is explained below. Suppose f is the total field and f_{res} is the residual. Initially, let $f_{res} = f$.

Step 1: calculate the mean value of f_{res} in the whole domain and denote it as $\bar{f}$ for domain-mean.

Step 2: update the residual, $f_{res} = f - \bar{f}$, calculate the mean value of f_{res} over a coarse grid with 2000 km spacing, and denote it as f^p for planetary-scale fluctuations.

Step 3: update the residual, $f_{res} = f - \bar{f} - f^p$, calculate the mean value of f_{res} over a coarse grid with 256 km spacing, and denote it as f^* for synoptic-scale fluctuations.

Step 4: update the residual, $f_{res} = f - \bar{f} - f^p - f^*$, calculate the mean value of f_{res} over a coarse grid with 16 km spacing, and denote it as f' for mesoscale fluctuations.

The coarse grid spacing (2000 km, 256 km, 16 km) is chosen so that 10 coarse grids (20000 km, 2560 km, 160 km) are able to resolve planetary-, synoptic- and meso-scale fluctuations, respectively. In practice, we first coarse grain the total fields onto coarse grids of 16 km to save computing expense and filter out fluctuations on smaller scales below 16 km. Such a residual based technique for multi-scale decomposition is similar to that in Brenowitz et al. (2018), except that the latter uses the low-pass filter in the Fourier domain. Fig.4 gives an example for decomposing brightness temperature from the non-rotating case by using this multi-scale decomposition method. This method successfully captures the spatio-temporal variability of convection across multiple scales, including eastward-moving planetary-scale envelopes in panel (b), synoptic-scale eastward- and westward-moving disturbances in panel (d) and prevalent westward-moving MCSs in panel (e). The domain mean field in panel (c) is steady with negligible variance.

4. The ITCZ Regime with Weak Rotation

In this section, we focus on the ITCZ regime with weak rotation ($0 \sim 6^\circ$ N). Typical regions in this regime include the warm pool region from the Indian Ocean to the West Pacific and the ITCZ region over the East Pacific (Waliser and Gautier 1993; Yang et al. 2017). Here we first derive a multi-scale model with weak rotation across the planetary-, synoptic- and meso-scales by following the systematic multi-scale asymptotic theory (Majda and Klein 2003; Majda 2007). Then we use it as a diagnostic framework for energy budget analysis to understand why planetary-scale organization of convection diminishes in this regime, as shown by Fig. 1a-d.

a. A multi-scale model with weak rotation for interactions of convection across planetary-, synoptic- and meso-scales

In general, multi-scale asymptotic models are useful for capturing leading-order scale interactions of convection across multiple spatial and temporal scales (Yang and Majda 2014; Majda and Yang 2016; Yang et al. 2017). The derivation of this multi-scale model starts from the 2-D anelastic primitive equations on the f plane. The Froude number $\varepsilon = 0.1$ is chosen as the small parameter for multi-scale asymptotic analysis. According to the standard scaling (Majda 2007), synoptic-scale spatial and temporal coordinates (x,t) have dimensional units of $(1500km, 8.3hrs)$. Correspondingly, the planetary-scale spatial and temporal coordinates (X,T) have dimensional units $(15000km, 3days)$ that are $\frac{1}{\varepsilon} = 10$ times of synoptic scales, while meso-scale coordinates (x', τ) are $\varepsilon = \frac{1}{10}$ of synoptic scales. As for physical variables, zonal and meridional velocity, (u, v), are scaled in a unit of 50 ms^{-1}, and vertical velocity w in a unit of 0.16 ms^{-1}. Pressure perturbation p is scaled in a unit of 2500 m^2s^{-2}, potential temperature anomalies θ and moisture anomalies q in a unit of 15 K, and diabatic heating s_θ in a unit of 45 $Kday^{-1}$. The order of variables are summarized in the third column of Table 2. In order to separate terms into different scales, spatial averaging operator $\overline{u}$ and temporal averaging operator $\langle u \rangle$ for an arbitrary variable u, and the superscripts p, s indicates the averaging on planetary and synoptic scales, respectively.

This multi-scale model consists of four groups of equations, each of which governs dynamics on one specific spatial temporal scales. In detail, the first group of equations at the 3rd row of Table 2 describe trade wind dynamics on the planetary/intraseasonal scale as a climatological background. In contrast, the second group of equations at the 4th row describes the planetary/intraseasonal anomalies under the effects of rotation, which are also influenced by the advection of background flow U, W and interaction terms involving trade wind fields, U, Θ, Q. Furthermore, the eddy transfer of zonal momentum from synoptic fluctuations, $-\rho_0^{-1}\left(\rho_0 \langle \overline{w^* u^*} \rangle^p\right)_z$ and that from mesoscale fluctuations, $-\rho_0^{-1}\left(\rho_0 \langle \overline{w' u'} \rangle^p\right)_z$ represent upscale impact of synoptic- and meso-scale dynamics. Similar eddy terms also appear at the right hand side of meridional momentum, potential temperature, and moisture equations. The third group of equations at the 5th row govern the dynamics of synoptic-scale fluctuations, which is affected by the trade wind fields as well as eddy terms from mesoscale fluctuations. The last group of equations at the 6th row describe the dynamics of mesoscale fluctuations advected by trade wind fields.

b. Effects of eddy momentum transfer on planetary-scale momentum and kinetic energy budget

According to the governing equations for planetary-scale zonal and meridional momentum in Table 2,

$$\frac{Du}{DT} + uU_X + wU_z - \hat{f}V = -p_X - \hat{d}u - \rho_0^{-1}\left(\rho_0 \left\langle \overline{w^* u^*} \right\rangle^p\right)_z - \rho_0^{-1}\left(\rho_0 \left\langle \overline{w' u'} \right\rangle^p\right)_z, \quad (1)$$

$$\frac{DV}{DT} + \hat{f}u = -\hat{d}V - \rho_0^{-1}\left(\rho_0 \left\langle \overline{w^* v^*} \right\rangle^p\right)_z - \rho_0^{-1}\left(\rho_0 \left\langle \overline{w' v'} \right\rangle^p\right)_z, \quad (2)$$

where the trade wind background U is assumed to be -10 ms^{-1}. After taking the climatological-mean $[\cdot]$ (zonal and time averaging), the above equations are rewritten as,

$$[u_T] = \left[\hat{f}V\right] + \left[-\hat{d}u\right] + \left[-\rho_0^{-1}\left(\rho_0 \left\langle \overline{w^* u^*} \right\rangle^p\right)_z\right] + \left[-\rho_0^{-1}\left(\rho_0 \left\langle \overline{w' u'} \right\rangle^p\right)_z\right], \quad (3)$$

$$[V_T] = \left[-\hat{f}u\right] + \left[-\hat{d}V\right] + \left[-\rho_0^{-1}\left(\rho_0 \left\langle \overline{w^* v^*} \right\rangle^p\right)_z\right] + \left[-\rho_0^{-1}\left(\rho_0 \left\langle \overline{w' v'} \right\rangle^p\right)_z\right], \quad (4)$$

which indicate that eddy momentum transfer from synoptic- and meso-scale fluctuations influences the planetary-scale winds.

Fig. 5a-c show the climatological-mean vertical profiles of eddy zonal momentum transfer from meso-, synoptic- and planetary-scale fluctuations. In detail, the eddy momentum transfer from mesoscale fluctuations in panel (a) induces westward (eastward) momentum forcing in the lower (middle and upper) tropospheres. Its magnitude gets weakened in both the upper and lower tropospheres as the latitude increases. In contrast, eddy momentum transfer from synoptic-scale fluctuations in panel (b) is negligible, while that from planetary-scale fluctuations in panel (c) has significant momentum forcing only above 600 hPa. In addition, panel (d) and (e) show the Coriolis force term and momentum drag, both of which have the opposite vertical profiles as that in panel (a). As the latitude increases, the momentum damping effect in panel (d) gets strengthened, while that in panel (e) gets weakened.

Fig. 6(a-c) shows the climatological-mean vertical profiles of eddy meridional momentum transfer from meso-, synoptic- and planetary-scale fluctuations. In detail, the eddy meridional momentum transfer from mesoscale fluctuations induces both low-level and middle-tropospheric southward momentum forcing and upper-tropospheric northward momentum forcing, while that from synoptic fluctuations is negligible. The eddy momentum transfer from planetary-scale fluctuations induces northward momentum forcing in the upper troposphere and southward momentum force near the tropopause. The Coriolis force and momentum damping in panels (d) and (e) have the similar vertical profiles but in the opposite signs.

After multiplying Eqs. 1 and 2 by $\rho_0 u$ and $\rho_0 v$ respectively and taking climatological mean, we can obtain the planetary kinetic energy budget equations,

$$\left[\left(\frac{1}{2}\rho_0 u^2\right)_T\right] = \left[\rho_0 \hat{f} V u\right] + \left[-\rho_0 p_X u\right] + \left[-\hat{d}\rho_0 u^2\right] + \left[-\left(\rho_0 \left\langle \overline{w^* u^*}\right\rangle^p\right)_z u\right] + \left[-\left(\rho_0 \left\langle \overline{w' u'}\right\rangle^p\right)_z u\right], \quad (5)$$

$$\left[\left(\frac{1}{2}\rho_0 V^2\right)_T\right] = \left[-\rho_0 \hat{f} u V\right] + \left[-\hat{d}\rho_0 V^2\right] + \left[-\left(\rho_0 \left\langle \overline{w^* v^*}\right\rangle^p\right)_z V\right] + \left[-\left(\rho_0 \left\langle \overline{w' v'}\right\rangle^p\right)_z V\right]. \quad (6)$$

Fig.7a-c show the vertical profiles of energy source and sink terms in the planetary-scale kinetic energy budget for zonal winds. Panel (a) shows the deceleration term involving the Coriolis force, which transfers kinetic energy from zonal winds to meridional winds. In contrast, both terms involving synoptic- and meso-scale fluctuations in panels (b) and (c) induce acceleration effects in both lower and upper tropospheres, whose magnitudes decrease gradually as the latitude increases. Fig. 7d-f are for meridional winds. As shown by panel (e), the term involving eddy momentum transfer from synoptic-scale fluctuations is negligible at levels below 400 hPa but induces acceleration/deceleration effects above that level. In contrast, the term involving eddy meridional momentum transfer from mesoscale fluctuations in panel (f) always induces deceleration effects throughout the troposphere.

Fig. 8a-b show the planetary-scale kinetic energy budget for zonal and meridional winds. The first term for time tendency has negligible value in both panels. As shown by panel (a), eddy momentum transfer from both synoptic- and meso-scale fluctuations induce acceleration effect, while the terms involving the Coriolis force, pressure gradient and momentum damping induce deceleration effect. As the latitude increases from 0 deg to 1,3,5 deg, acceleration effect induced by both eddy momentum transfer term gets weakened, while the Coriolis force term increases dramatically. Besides, both the terms involving pressure gradient and damping decrease as the latitude increases. As shown by panel (b), the term involving eddy meridional momentum transfer from synoptic-scale fluctuations induces weak acceleration effect, while that from mesoscale fluctuations and the damping term induce significant deceleration effect.

Fig. 9a shows the schematic diagram for planetary-scale kinetic energy budget in the weak rotation regime. According to Fig.8a, the dominant acceleration effect comes from the term involving eddy zonal momentum transfer from mesoscale fluctuations $\left[-\left(\rho_0\left\langle\overline{w'u'}\right\rangle^p\right)_z u\right]$, while the dominant deceleration effect comes from the term involving the Coriolis force $\left[\rho_0\hat{f}Vu\right]$. As the magnitude of rotation increases, this acceleration effect decreases dramatically while the deceleration effect increases instead. The resulting reduced planetary-scale kinetic energy budget of zonal winds explains the diminishing planetary-scale organized convection.

Both changed acceleration/deceleration effects should be traced back to the increasing magnitude of rotation, as it is the only difference in the model input. In fact, the increasing deceleration term $\left[\rho_0\hat{f}Vu\right]$ can be simply explained by the larger value of f at higher latitudes. As for the acceleration term $\left[-\left(\rho_0\left\langle\overline{w'u'}\right\rangle^p\right)_z u\right]$, its decreasing strength is attributed to less favorable conditions for MCSs provided by background sounding of both low-level equivalent potential temperature and low-level vertical shear of zonal winds as shown in Fig. 9b. According to Fig. 3f, the low-level equivalent potential temperature between 600-800 hPa increases by a few Kelvin as the magnitude of rotation increases, leading to larger convective inhibition (CIN) and less moist instability. Meanwhile, the Coriolis term fV in Fig. 5d induces a momentum forcing in the opposite sign as the climatological mean zonal winds in Fig. 3a, resulting in reduced low-level vertical shear.

c. Effects of eddy heat transfer on planetary-scale heat and available potential energy budget

The governing equation for planetary-scale potential temperature anomalies in Table 2 reads as follows,

$$\theta_T + U\theta_X + N^2 w = -\hat{d}_\theta \theta - \rho_0^{-1}\left(\rho_0 \left\langle \overline{w^*\theta^*} \right\rangle^p\right)_z - \rho_0^{-1}\left(\rho_0 \left\langle \overline{w'\theta'} \right\rangle^p\right)_z + s_\theta, \quad (7)$$

where the trade wind background is assumed to be $U = -10ms^{-1}$ and $\Theta = 0K$. The corresponding climatological-mean equation is,

$$[\theta_T] = \left[-N^2 w\right] + \left[-\hat{d}_\theta \theta\right] + \left[-\rho_0^{-1}\left(\rho_0 \left\langle \overline{w^*\theta^*} \right\rangle^p\right)_z\right] + \left[-\rho_0^{-1}\left(\rho_0 \left\langle \overline{w'\theta'} \right\rangle^p\right)_z\right] + [s_\theta]. \quad (8)$$

Fig.10 show the climatological-mean vertical profiles of eddy heat transfer from meso-, synoptic- and planetary-scale fluctuations. Unlike Fig. 5 and 6, the vertical profiles of all eddy terms do not change much as the latitude increases, indicating that these terms are not directly responsible for the diminishment of planetary-scale organization of convection. In fact, both eddy heat transfer from synoptic- and meso-scale fluctuations introduces heating in the lower troposphere and increases CIN, providing unfavorable conditions for convection. In contrast, the eddy heat transfer from planetary-scale fluctuations in panel (c) only induces heating/cooling effects above 500 hPa.

After multiplying Eq.7 by $\frac{\rho_0\theta}{N^2}$ and taking climatological mean, the governing equation for available potential energy budget is obtained below,

$$\left[\left(\rho_0\frac{\theta^2}{2N^2}\right)_T\right]=[-\rho_0 w\theta]+\left[-\rho_0\hat{d}_\theta\frac{\theta^2}{N^2}\right]+\left[-\left(\rho_0\left\langle\overline{w^*\theta^*}\right\rangle^p\right)_z\frac{\theta}{N^2}\right]+\left[-\left(\rho_0\left\langle\overline{w'\theta'}\right\rangle^p\right)_z\frac{\theta}{N^2}\right]+\left[\rho_0 s_\theta\frac{\theta}{N^2}\right], \tag{9}$$

where the term $[-\rho_0 w\theta]$ transfers energy between kinetic energy and available potential energy.

Fig.11 shows the climatological-mean vertical profiles of energy source and sink terms in available potential energy budget. The energy transfer term in panel (a) is characterized by the second baroclinic mode with upper-tropospheric (lower-tropospheric) energy sink (source) in a decreasing magnitude. As shown by panels (b) and (c), the energy source/sink terms involving eddy heat transfer from synoptic- and meso-scale fluctuations share the similar vertical profiles, both of which feature an energy source below 850 hPa and above 300 hPa, and an energy sink between 350-850 hPa. Meanwhile, neither term changes much throughout the troposphere as the latitude increases, indicating that these terms are not directly responsible for the diminishing planetary-scale organization.

d. Effects of eddy transfer of equivalent potential temperature on the planetary-scale atmospheric stability

Similar to Eq.8, the governing equation for equivalent potential temperature, θ_e, reads as follows,

$$[(\theta_e)_T]=\left[-N_e^2 w\right]+\left[-\hat{d}_\theta\theta_e\right]+\left[-\rho_0^{-1}\left(\rho_0\left\langle\overline{w^*\theta_e^*}\right\rangle^p\right)_z\right]+\left[-\rho_0^{-1}\left(\rho_0\left\langle\overline{w'\theta_e'}\right\rangle^p\right)_z\right], \tag{10}$$

where N_e represents background stratification of equivalent potential temperature.

Fig.12 shows the climatological-mean vertical profiles of eddy transfer of equivalent potential temperature from planetary-, synoptic- and meso-scale fluctuations. Among these three terms, eddy terms from synoptic- and meso-scale fluctuations dominate and induce cooling and drying effects below 850 hPa and heating and moistening effects above that level. The eddy term from planetary fluctuations have negligible magnitude throughout the troposphere. As shown by panel (d), the total eddy heat transfer features significant positive vertical gradient in the lower troposphere, which tends to reduce the atmospheric instability and provide unfavorable conditions for convection. It is worth mentioning that these vertical profiles do not change as the magnitude of rotation increases.

5. The Indian Monsoon Regime with Order-One Rotation

In this section, we will focus on the Indian Monsoon regime with order-one rotation ($6^\circ \sim 20^\circ N$). A typical region in this regime is the monsoon trough over the Indian subcontinent (Gadgil 2003). As shown by Fig.1e-g, large-scale convection is dominated by synoptic-scale envelopes that move eastward at a speed of 15 m/s, resembling the simulation by Grabowski and Moncrieff (2001). It is important to investigate the upscale impact of MCSs on synoptic-scale dynamics and understand why synoptic-scale organization persists in this regime.

Table 3 shows the multi-scale model for the scale interactions across meso-, synoptic- and planetary-scales in the order-one rotation regime. To derive this multi-scale model, we use the same physical scaling for all physical variables as Section 4a, except for the Coriolis force parameter f in the order-one magnitude. Thus, the two models in Table 2 and 3 share many similar features. The major difference lies in the fact that trade wind background and synoptic-scale dynamics in Table 3 feel the Coriolis force. Moreover, this three-scale model can be regarded as the coupling between the IMMD model (Biello and Majda 2010) for planetary- and synoptic-scale interactions and the MESD model (Majda 2007) for synoptic- and meso-scale interactions.

Upscale impact of meso-scale fluctuations on synoptic-scale dynamics

According to Table 3, synoptic-scale dynamics is driven by eddy transfer of momentum, temperature and moisture from mesoscale fluctuations. It should be interesting to investigate the upscale impact of MCSs on synoptic-scale organization of convection in this regime. The governing equations for synoptic-scale kinetic energy budget of zonal and meridional winds and available potential energy budget read below,

$$\left[\left(\frac{1}{2}\rho_0(u^*)^2\right)_t\right] = \left[\rho_0\hat{f}v^*u^*\right] + \left[-\rho_0 p_x^* u^*\right] + \left[-\left(\rho_0\left\langle\overline{w'u'}\right\rangle^s\right)_z u^*\right], \quad (11)$$

$$\left[\left(\frac{1}{2}\rho_0(v^*)^2\right)_t\right] = \left[-\rho_0\hat{f}v^*u^*\right] + \left[-\left(\rho_0\left\langle\overline{w'v'}\right\rangle^s\right)_z v^*\right], \quad (12)$$

$$\left[\left(\rho_0\frac{(\theta^*)^2}{2N^2}\right)_t\right] = \left[-\rho_0 w^*\theta^*\right] + \left[-\left(\rho_0\left\langle\overline{w'\theta'}\right\rangle^s\right)_z\frac{\theta^*}{N^2}\right] + \left[\rho_0 s_\theta^*\frac{\theta^*}{N^2}\right]. \quad (13)$$

Fig.13 shows the climatological-mean vertical profiles of energy source/sink terms on the synoptic-scale kinetic and available potential energy budgets. It turns out that eddy zonal momentum transfer in panel (a) induces acceleration effects throughout the troposphere, whose magnitude decays gradually as the latitude increases. In contrast, eddy meridional momentum transfer in panel (b) induces weaker deceleration effects, while eddy heat transfer in panel (c) induces alternate energy source and sink at different levels. Besides, the Coriolis force term in panel (d) transfers kinetic energy from zonal winds to meridional winds, leading to deceleration effect in the kinetic energy budget of zonal winds. The term involving pressure gradient in panel (e) induces acceleration (deceleration) effect below (above) 850 hPa. In addition, the energy transfer term between kinetic and available potential energy in panel (f) is characterized by the second baroclinic mode with low-level (upper-level) energy source (sink).

Fig.14 shows the synoptic-scale kinetic energy budget for zonal and meridional winds. The time tendency term in both panels (a) and (b) has negligible value. The acceleration/deceleration effects induced by the Coriolis force do not change much. As for kinetic energy of zonal winds in panel (a), the dominant acceleration effect due to eddy zonal momentum transfer from mesoscale fluctuations decays as the latitude increases. Correspondingly, the deceleration effect due to pressure gradient also decays. As for meridional winds, the acceleration effect induced by the Coriolis force is balanced by the term involving eddy meridional momentum transfer and the damping residual. The residual in panel (b) is too large to be ignored and behaves as momentum dissipation, presumably due to the frictional effect from unorganized convection below the mesoscale that has been excluded in the budget analysis.

Fig.15 shows the schematic diagram for synoptic-scale kinetic energy budget. According to Fig. 14a, the dominant acceleration effect in synoptic kinetic energy of zonal winds is induced by eddy zonal momentum transfer from mesoscale fluctuations $\left[-\left(\rho_0\left\langle\overline{w'u'}\right\rangle^s\right)_z u^*\right]$, while the deceleration effect comes from the term involving the Coriolis force $\left[\rho_0\hat{f}v^*u^*\right]$. Thus, this acceleration effect maintains the synoptic-scale organization of convection. As the latitude further increases, this acceleration effect decays gradually, while the deceleration effect is unchanged. The resulting reduced synoptic-scale kinetic energy of zonal winds explains the diminishment of synoptic-scale organization in the order-one and strong rotation regimes in Fig. 1e-h. Similar to the weak rotation regime, the decaying upscale impact of MCSs is attributed to less favorable conditions for convection provided by background sounding of warmer low-level equivalent potential temperature and weaker low-level vertical shear of zonal winds at higher latitudes, as shown in Fig. 3.

6. The Mid-Latitude Regime with Strong Rotation

In this section, we consider the mid-latitude regime with strong rotation. As shown by Fig.1h, the solution in this regime is characterized by scattered and random MCSs prevailing in the whole domain. It is interesting to investigate the upscale impact of MCSs and understand the vanishment of synoptic-scale organization of convection in the strong rotation regime.

a. A multi-scale model with strong rotation for interactions of convection across planetary-, synoptic- and meso-scales

It is well known that large-scale circulation at mid-latitudes is governed by the QG dynamics. Thus the standard QG scaling (Vallis 2017) is adopted here. In details, synoptic-scale spatial and temporal coordinates (x,t) have dimensional units of $(1000km, 28hrs)$. Correspondingly, the planetary-scale spatial coordinate X has dimensional units $10000km$ that are $\frac{1}{\varepsilon} = 10$ times of those on the synoptic scale, while meso-scale coordinates (x', τ) are $\varepsilon = \frac{1}{10}$ of synoptic-scale ones. As for physical variables, zonal and meridional velocity, (u, v), are scaled in a unit of 10 ms^{-1}, and vertical velocity w in a unit of 0.1 ms^{-1}. Pressure perturbation p is scaled in a unit of 1000 m^2s^{-2}, potential temperature anomalies θ and moisture anomalies q in a unit of 3 K, and diabatic heating s_θ in a unit of 2.57 $Kday^{-1}$.

Table 4 shows the multi-scale model in this strong rotation regime with three groups of equations, each of which governs one single scale dynamics. In brief, the planetary-scale dynamics is governed by long-wave approximation equations, the synoptic-scale dynamics is governed by QG equations, and the mesoscale dynamics is governed by the linear mesoscale equatorial weak temperature gradient (MEWTG) equations (Majda and Klein 2003; Majda et al. 2008). Notably, this multi-scale model is distinguished from the other two models in Table 2 and 3 by the absence of eddy terms across planetary-, synoptic- and meso-scales. This multi-scale model predicts theoretically that upscale impact of synoptic- and meso-scale fluctuations is negligible in the strong rotation regime.

b. Upscale impact of meso-scale fluctuations on synoptic-scale dynamics

Fig. 16 shows the synoptic-scale kinetic energy budget for zonal and meridional winds in the strong rotation regime. The overall features of all energy source and sink terms are similar to those in Fig.14. In particular, eddy zonal momentum transfer from meso-scale fluctuations still induces acceleration effect in the kinetic energy budgets, whose magnitude further decreases as the latitude increases. In contrast, eddy meridional momentum transfer induces deceleration effects. However, when compared with Fig.14, these acceleration/deceleration effects are too weak to support synoptic-scale organization of convection. Unlike Fig.14, the deceleration effect due to the Coriolis force gradually decreases as the rotation increases.

7. Concluding Discussion

This study is aimed at investigating the effects of rotation on the multi-scale organization of convection with the following goals. First, we use a global 2-D CRM to simulate multi-scale organization of convection in three rotation regimes (weak, order-one, and strong), representing idealized ITCZ region ($0^\circ \sim 6^\circ$ N), Indian monsoon region ($6^\circ \sim 20^\circ$ N), and mid-latitude region ($20^\circ \sim 45^\circ$ N), respectively. Secondly, we derive a multi-scale asymptotic model for upscale and downscale impacts in each rotation regime and use it as a diagnostic framework for energy budget analysis. Thirdly, we explain why planetary-scale organization diminishes in the weak rotation regime as the magnitude of rotation increases and investigate the role of eddy transfer of momentum, temperature, and equivalent potential temperature from meso- and synoptic-scale fluctuations. Lastly, we explain why synoptic-scale organization persists in the order-one rotation regime but diminishes in the strong rotation regime.

Here we use the 2-D version of the SAM model to simulate multi-scale organization of convection with different magnitudes of rotation. In the weak rotation regime, planetary-scale organization of convection arises at the latitude 0 deg and 1° N, but diminishes as the magnitude of rotation increases. The eastward-moving planetary-scale envelope contains several eastward- and westward-moving synoptic-scale disturbances with numerous embedded MCSs. In the order-one rotation regime, convection is organized in a two-scale structure with eastward-moving synoptic-scale envelopes and westward-moving embedded MCSs. In the strong rotation regime, numerous scattered and unorganized MCSs prevail in the whole domain. The effect of rotation on large-scale organization of convection as revealed by this CRM simulation is consistent to that in Majda et al. (2015). With both radiative cooling and surface fluxes fixed, the planetary-scale organization of convection in our simulations is mainly due to the multi-scale interactions of flow fields, distinguishing itself from several previous theories that focus on convection-radiation-surface fluxes feedbacks. (Bretherton et al. 2005; Wing and Emanuel 2014; Bretherton and Khairoutdinov 2015).

Here we divide all scenarios into three regimes (weak, order-one, and strong) in terms of the magnitude of rotation. In each rotation regime, a three-scale model is derived by using the multi-scale asymptotic method and used as a diagnostic framework to study the scale interactions of convection across planetary-, synoptic- and meso-scales. Although they are reduced models from the primitive equations, these multi-scale models presumably capture the leading-order quantities of all flow fields with only small errors. The advantages of using these multi-scale models as a diagnostic framework for budget analysis lie in three aspects, including i) modeling the scale interactions of flow fields across multiple scales, ii) highlighting possible dominant terms in the energy budget, iii) simplifying the diagnostic studies by ignoring secondary terms. By diagnostically calculating energy budget based on these multi-scale models, we figure out energy transfer routes on both planetary and synoptic scales and summarize them in the schematic diagrams in Fig. 9a and Fig. 15. As shown by Fig. 9a, planetary kinetic energy of zonal winds is fueled by dominant acceleration effect from MCSs and also that from synoptic convectively coupled waves, but consumed through energy transfer to kinetic energy of meridional winds and available potential energy as well as dissipation. The energy transfer routes on synoptic scale in Fig. 15 are similar to those on planetary scale, reflecting the self-similarity property of convection (Majda 2007).

The results here highlight the crucial upscale impact of eddy zonal momentum transfer from mesoscale fluctuations on both planetary- and synoptic-scale organization of convection. As the magnitude of rotation increases, its acceleration effect on the planetary kinetic energy of zonal winds decreases gradually, diminishing the planetary-scale organization of convection. Similarly, due to its decreasing acceleration effect on synoptic kinetic energy of zonal winds, synoptic-scale organization of convection only persists in the order-one rotation regime but diminishes in the strong rotation regime. This indicates a need to parameterize upscale impact of MCSs in the coarse-resolution GCMs. In fact, the MESD model (Majda 2007) theoretically predicts the significant upscale impact of MCSs on eastward-moving CCKWs (Yang and Majda 2017, 2018) and 2-day waves (Yang and Majda 2019). Based on the explicit expressions of eddy terms obtained from the MESD model, Yang et al. (2019) proposed a basic parameterization of upscale impact of upshear-moving MCSs and showed that this parameterization significantly improves key features of the MJO analog in a multicloud model. Moncrieff et al. (2017) introduced a parameterization for collective effects of mesoscale organized convection that are missing in the contemporary cumulus parameterization in the GCM.

The diminishing acceleration effects from MCSs are traced back to the increasing magnitude of rotation, since it is the only difference in the model input among all simulations. As the magnitude of rotation increases, both vertical gradient of equivalent potential temperature and vertical shear of zonal winds in the lower troposphere decays, providing less favorable conditions for the generation and propagation of MCSs. Consequently, their upscale impact on the planetary and synoptic kinetic energy diminishes. The schematic diagram in Fig. 9b specifically depicts the effects of increasing rotation on background sounding with less favorable conditions for promoting MCSs. Such upscale and downscale impacts illustrate the crucial role of multi-scale interactions in scale selection and organization of convection. Studying the effects of rotation should help improve our fundamental understanding of large-scale organization of convection at different latitudes. Besides, the MCSs in this 2-D CRM with rotation share several realistic features with 3-D CRMs, while those in 2-D CRMs without rotation typically have an unrealistic strong circulation in the zonal direction.

This study can be elaborated and extended in various ways. The implication of multi-scale organization of convection presented here is limited due to the 2-D model configuration. Thus one research direction is to implement the 3-D simulations and investigate the effects of rotation. Meanwhile, the validity of using multi-scale asymptotic models as a diagnostic framework depends on appropriate physical scaling for all flow fields and a good multi-scale decomposition method for capturing the scale separation property of solutions. Another research direction is to consider the multi-scale interactions of convection over the warm pool scenario. Also, it should be interesting to consider the scenario in the presence of active radiation and surface flux and investigate whether the multi-scale interaction mechanism would collaborate with the convection-radiation-surface flux feedback mechanisms.

Acknowledgments. This research of A.J.M. is partially supported by the office of Naval Research ONR MURI N00014-12-1-0912 and the Center for Prototype Climate Modeling (CPCM) in New York University Abu Dhabi (NYUAD) Research Institute. Q.Y. is funded as a postdoctoral fellow by CPCM in NYUAD Research Institute. N.B. is supported as a postdoctoral fellow by the Washington Research Foundation and by a Data Science Environments project award from the Gordon and Betty Moore Foundation (Award 2013-10-29) and the Alfred P. Sloan Foundation (Award 3835) to the University of Washington eScience Institute.

References

Back, A., and J. A. Biello, 2018: Effect of overturning circulation on long equatorial waves: A low-frequency cutoff. *J. Atmos. Sci.*, **75 (5)**, 1721–1739.

Biello, J. A., and A. J. Majda, 2010: Intraseasonal multi-scale moist dynamics of the tropical atmosphere. *Communications in Mathematical Sciences*, **8 (2)**, 519–540.

Brenowitz, N., A. Majda, and Q. Yang, 2018: The multiscale impacts of organized convection in global 2-d cloud-resolving models. *JAMES*, **10 (8)**, 2009–2025.

Bretherton, C. S., P. N. Blossey, and M. Khairoutdinov, 2005: An energy-balance analysis of deep convective self-aggregation above uniform sst. *J. Atmos. Sci.*, **62 (12)**, 4273–4292.

Bretherton, C. S., and M. F. Khairoutdinov, 2015: Convective self-aggregation feedbacks in near-global cloud-resolving simulations of an aquaplanet. *JAMES*, **7 (4)**, 1765–1787.

Chen, S. S., R. A. Houze, Jr., and B. E. Mapes, 1996: Multiscale variability of deep convection in realation to large-scale circulation in TOGA COARE. *J. Atmos. Sci.*, **53 (10)**, 1380–1409.

Deng, Q., B. Khouider, and A. J. Majda, 2015: The MJO in a coarse-resolution gcm with a stochastic multicloud parameterization. *J. Atmos. Sci.*, **72 (1)**, 55–74.

Gadgil, S., 2003: The indian monsoon and its variability. *Annual Review of Earth and Planetary Sciences*, **31 (1)**, 429–467.

Goswami, B., B. Khouider, R. Phani, P. Mukhopadhyay, and A. J. Majda, 2017: Improving synoptic and intra-seasonal variability in CFSv2 via stochastic representation of organized convection. *Geophys. Res. Lett.*, **44 (2)**, 1104–1113.

Grabowski, W. W., and M. W. Moncrieff, 2001: Large-scale organization of tropical convection in two-dimensional explicit numerical simulations. *Quart. J. Roy. Meteor. Soc.*, **127 (572)**, 445–468.

Guichard, F., and F. Couvreux, 2017: A short review of numerical cloud-resolving models. *Tellus A: Dynamic Meteorology and Oceanography*, **69 (1)**, 1373 578.

Guo, Y., D. E. Waliser, and X. Jiang, 2015: A systematic relationship between the representations of convectively coupled equatorial wave activity and the madden–julian oscillation in climate model simulations. *JCLI*, **28 (5)**, 1881–1904.

Held, I. M., R. S. Hemler, and V. Ramaswamy, 1993: Radiative-convective equilibrium with explicit two-dimensional moist convection. *J. Atmos. Sci.*, **50 (23)**, 3909–3927.

Houze, R. A., Jr., 2004: Mesoscale convective systems. *Rev. Geophys.*, **42 (4)**.

Hurley, J. V., and W. R. Boos, 2015: A global climatology of monsoon low-pressure systems. *Quart. J. Roy. Meteor. Soc.*, **141 (689)**, 1049–1064.

Jiang, X., and Coauthors, 2015: Vertical structure and physical processes of the Madden-Julian oscillation: Exploring key model physics in climate simulations. *Journal of Geophysical Research: Atmospheres*, **120 (10)**, 4718–4748.

Khairoutdinov, M. F., and D. A. Randall, 2003: Cloud resolving modeling of the arm summer 1997 iop: Model formulation, results, uncertainties, and sensitivities. *J. Atmos. Sci.*, **60 (4)**, 607–625.

Khouider, B., J. Biello, and A. J. Majda, 2010: A stochastic multicloud model for tropical convection. *Communications in Mathematical Sciences*, **8 (1)**, 187–216.

Khouider, B., and A. J. Majda, 2006a: Model multi-cloud parameterizations for convectively coupled waves: Detailed nonlinear wave evolution. *Dyn. Atmos. Oceans*, **42 (1)**, 59–80.

Khouider, B., and A. J. Majda, 2006b: Multicloud convective parametrizations with crude vertical structure. *Theor. Comput. Fluid Dyn.*, **20 (5-6)**, 351–375.

Khouider, B., and A. J. Majda, 2006c: A simple multicloud parameterization for convectively coupled tropical waves. part I: Linear analysis. *J. Atmos. Sci.*, **63 (4)**, 1308–1323.

Khouider, B., and A. J. Majda, 2007: A simple multicloud parameterization for convectively coupled tropical waves. part II: Nonlinear simulations. *J. Atmos. Sci.*, **64 (2)**, 381–400.

Khouider, B., and A. J. Majda, 2008a: Equatorial convectively coupled waves in a simple multicloud model. *J. Atmos. Sci.*, **65 (11)**, 3376–3397.

Khouider, B., and A. J. Majda, 2008b: Multicloud models for organized tropical convection: Enhanced congestus heating. *J. Atmos. Sci.*, **65 (3)**, 895–914.

Kiladis, G. N., M. C. Wheeler, P. T. Haertel, K. H. Straub, and P. E. Roundy, 2009: Convectively coupled equatorial waves. *Rev. Geophys.*, **47 (2)**.

Kim, H., F. Vitart, and D. E. Waliser, 2018: Prediction of the madden–julian oscillation: A review. *J. Climate*, **31 (23)**, 9425–9443.

Liu, C., and M. W. Moncrieff, 2004: Effects of convectively generated gravity waves and rotation on the organization of convection. *J. Atmos. Sci.*, **61 (17)**, 2218–2227.

Majda, A. J., 2000: Real world turbulence and modern applied mathematics. *Mathematics: frontiers and perspectives*, 137–151.

Majda, A. J., 2007: New multiscale models and self-similarity in tropical convection. *J. Atmos. Sci.*, **64 (4)**, 1393–1404.

Majda, A. J., 2012: Climate science, waves and pdes for the tropics. *Nonlinear Partial Differential Equations*, Springer, 223–230.

Majda, A. J., B. Khouider, and Y. Frenkel, 2015: Effects of rotation and mid-troposphere moisture on organized convection and convectively coupled gravity waves. *Climate Dyn.*, **44 (3-4)**, 937–960.

Majda, A. J., and R. Klein, 2003: Systematic multiscale models for the tropics. *J. Atmos. Sci.*, **60 (2)**, 393–408.

Majda, A. J., M. Mohammadian, and Y. Xing, 2008: Vertically sheared horizontal flow with mass sources: a canonical balanced model. *Geophysical and Astrophysical Fluid Dynamics*, **102 (6)**, 543–591.

Majda, A. J., and Q. Yang, 2016: A multiscale model for the intraseasonal impact of the diurnal cycle over the maritime continent on the Madden–Julian oscillation. *J. Atmos. Sci.*, **73 (2)**, 579–604.

Miura, H., M. Satoh, T. Nasuno, A. T. Noda, and K. Oouchi, 2007: A Madden-Julian oscillation event realistically simulated by a global cloud-resolving model. *Science*, **318 (5857)**, 1763–1765.

Moncrieff, M., 1981: A theory of organized steady convection and its transport properties. *Quart. J. Roy. Meteor. Soc.*, **107**, 29–50.

Moncrieff, M. W., and C. Liu, 1999: Convection initiation by density currents: Role of convergence, shear, and dynamical organization. *Mon. Wea. Rev.*, **127 (10)**, 2455–2464.

Moncrieff, M. W., C. Liu, and P. Bogenschutz, 2017: Simulation, modeling, and dynamically based parameterization of organized tropical convection for global climate models. *J. Atmos. Sci.*, **74 (5)**, 1363–1380.

Muller, C. J., and I. M. Held, 2012: Detailed investigation of the self-aggregation of convection in cloud-resolving simulations. *J. Atmos. Sci.*, **69 (8)**, 2551–2565.

Nakazawa, T., 1988: Tropical super clusters within intraseasonal variations over the western pacific. *J. Meteor. Soc. Japan*, **66 (6)**, 823–839.

Newton, C. W., and H. Rodebush Newton, 1959: Dynamical interactions between large convective clouds and environment with vertical shear. *J. Meteor.*, **16 (5)**, 483–496.

Riemann-Campe, K., K. Fraedrich, and F. Lunkeit, 2009: Global climatology of convective available potential energy (cape) and convective inhibition (cin) in era-40 reanalysis. *Atmos. Res.*, **93 (1-3)**, 534–545.

Schneider, T., 2006: The general circulation of the atmosphere. *Annu. Rev. Earth Planet. Sci.*, **34**, 655–688.

Slawinska, J., O. Pauluis, A. J. Majda, and W. W. Grabowski, 2014: Multiscale interactions in an idealized walker circulation: Mean circulation and intraseasonal variability. *J. Atmos. Sci.*, **71 (3)**, 953–971.

Tao, W.-K., and M. W. Moncrieff, 2009: Multiscale cloud system modeling. *Rev. Geophys.*, **47 (4)**.

Tompkins, A. M., 2001: Organization of tropical convection in low vertical wind shears: The role of water vapor. *J. Atmos. Sci.*, **58 (6)**, 529–545.

Vallis, G. K., 2017: *Atmospheric and oceanic fluid dynamics*. Cambridge University Press.

Waliser, D. E., and C. Gautier, 1993: A satellite-derived climatology of the ITCZ. *J. Climate*, **6 (11)**, 2162–2174.

Wing, A. A., and T. W. Cronin, 2016: Self-aggregation of convection in long channel geometry. *Quart. J. Roy. Meteor. Soc.*, **142 (694)**, 1–15.

Wing, A. A., and K. A. Emanuel, 2014: Physical mechanisms controlling self-aggregation of convection in idealized numerical modeling simulations. *JAMES*, **6 (1)**, 59–74.

Yang, Q., and A. J. Majda, 2014: A multi-scale model for the intraseasonal impact of the diurnal cycle of tropical convection. *Theor. Comput. Fluid Dyn.*, **28 (6)**, 605–633.

Yang, Q., and A. J. Majda, 2017: Upscale impact of mesoscale disturbances of tropical convection on synoptic-scale equatorial waves in two-dimensional flows. *J. Atmos. Sci.*, **74 (9)**, 3099–3120.

Yang, Q., and A. J. Majda, 2018: Upscale impact of mesoscale disturbances of tropical convection on convectively coupled kelvin waves. *J. Atmos. Sci.*, **75 (1)**, 85–111.

Yang, Q., and A. J. Majda, 2019: Upscale impact of mesoscale disturbances of tropical convection on 2-day waves. *J. Atmos. Sci.*, **76 (1)**, 171–194.

Yang, Q., A. J. Majda, and B. Khouider, 2017: ITCZ breakdown and its upscale impact on the planetary-scale circulation over the eastern pacific. *J. Atmos. Sci.*, **74 (12)**, 4023–4045.

Yang, Q., A. J. Majda, and M. W. Moncrieff, 2019: Upscale impact of mesoscale convective systems and its parameterization in an idealized gcm for a mjo analog above the equator. *accepted by Journal of the Atmospheric Sciences*.

Zhang, C., 2005: Madden-Julian oscillation. *Rev. Geophys.*, **43 (2)**.

LIST OF TABLES

TABLE 1: Coriolis force parameter ($f = 2\Omega \sin(\phi)$) and the corresponding time scale ($\frac{1}{f}$) in these 10 cases.

Regime	Latitude (deg N)	Coriolis f (1/s)	$\frac{1}{f}$ (hrs)
No Rotation	0	0	∞
Weak Rotation	1	2.5×10^{-6}	109.1
	3	7.6×10^{-6}	36.4
	5	1.3×10^{-5}	21.9
Order-One Rotation	9	2.3×10^{-5}	12.2
	14	3.5×10^{-5}	7.9
	20	5.0×10^{-5}	5.6
Strong Rotation	27	6.6×10^{-5}	4.2
	35	8.4×10^{-5}	3.3
	45	1.0×10^{-4}	2.7

TABLE 2: Multi-scale asymptotic model across planetary-, synoptic- and meso-scales in the weak rotation regime.

Regime 1: Weak Rotation ($\hat{f}$ from $\mathscr{O}(\varepsilon)$)		
Space and Time Scales	Governing Equations	Variables
Trade winds (planetary / intraseasonal)	$\frac{DU}{DT} = -P_X - \hat{d}(U - U_0)$ $\frac{D\Theta}{DT} + N^2 W = -\hat{d}_\theta \Theta + S_\theta$ $P_z = \Theta$ $U_X + \rho_0^{-1}(\rho_0 W)_z = 0$ $\frac{DQ}{DT} - Q_0 W = -S_\theta$	$\hat{d}, \hat{d}_\theta$ from $\mathscr{O}(\varepsilon)$ $\frac{D}{DT} = \frac{\partial}{\partial T} + U\frac{\partial}{\partial X} + W\frac{\partial}{\partial z}$ U, P, Θ, Q from $\mathscr{O}(1)$ V, W, S_θ from $\mathscr{O}(\varepsilon)$ $\rho_0 = \rho_0(z)$
Planetary / intraseasonal anomalies from the climatology	$\frac{Du}{DT} + uU_X + wU_z - \hat{f}V = -p_X - \hat{d}u$ $\quad -\rho_0^{-1}\left(\rho_0 \langle \overline{w^* u^*} \rangle^p\right)_z - \rho_0^{-1}\left(\rho_0 \langle \overline{w' u'} \rangle^p\right)_z$ $\frac{DV}{DT} + \hat{f}u = -\hat{d}V$ $\quad -\rho_0^{-1}\left(\rho_0 \langle \overline{w^* v^*} \rangle^p\right)_z - \rho_0^{-1}\left(\rho_0 \langle \overline{w' v'} \rangle^p\right)_z$ $\frac{D\theta}{DT} + u\Theta_X + w\Theta_z + N^2 w = -\hat{d}_\theta \theta + s_\theta$ $\quad -\rho_0^{-1}\left(\rho_0 \langle \overline{w^* \theta^*} \rangle^p\right)_z - \rho_0^{-1}\left(\rho_0 \langle \overline{w' \theta'} \rangle^p\right)_z$ $p_z = \theta$ $u_X + \rho_0^{-1}(\rho_0 w)_z = 0$ $\frac{Dq}{DT} + uQ_X + wQ_z - Q_0 w = -s_\theta$ $\quad -\rho_0^{-1}\left(\rho_0 \langle \overline{w^* q^*} \rangle^p\right)_z - \rho_0^{-1}\left(\rho_0 \langle \overline{w' q'} \rangle^p\right)_z$	$N^2 = 1$ u, V, p, θ, q from $\mathscr{O}(\varepsilon)$ w, s_θ from $\mathscr{O}(\varepsilon^2)$
Synoptic fluctuations in space or time	$u_t^* + Uu_x^* + w^* U_z = -p_x^* - \rho_0^{-1}\left(\rho_0 \langle \overline{w' u'} \rangle^s\right)_z$ $v_t^* + Uv_x^* = -\rho_0^{-1}\left(\rho_0 \langle \overline{w' v'} \rangle^s\right)_z$ $\theta_t^* + U\theta_x^* + w^*\Theta_z + N^2 w^* = -\rho_0^{-1}\left(\rho_0 \langle \overline{w' \theta'} \rangle^s\right)_z + s_\theta^*$ $p_z^* = \theta^*$ $u_x^* + \rho_0^{-1}(\rho_0 w^*)_z = 0$ $q_t^* + Uq_x^* + w^* Q_z - Q_0 w^* = -s_\theta^* - \rho_0^{-1}\left(\rho_0 \langle \overline{w' q'} \rangle^s\right)_z$	all variables from $\mathscr{O}(\varepsilon)$
Mesoscale fluctuations in space and time	$u'_\tau + Uu'_{x'} + w' U_z = -p'_{x'}$ $v'_\tau + Uv'_{x'} = 0$ $\theta'_\tau + U\theta'_{x'} + w'\Theta_z + N^2 w' = s'_\theta$ $p'_z = \theta'$ $u'_{x'} + \rho_0^{-1}(\rho_0 w')_z = 0$ $q'_\tau + Uq'_{x'} + w' Q_z - Q_0 w' = -s'_\theta$	u', v', p', θ', q' from $\mathscr{O}(\varepsilon)$ w', s'_θ from $\mathscr{O}(1)$

TABLE 3: Multi-scale asymptotic model across planetary-, synoptic- and meso-scales in the order-one rotation regime.

Regime 2: Order-One Rotation ($\hat{f}$ from $\mathcal{O}(1)$)		
Space and Time Scales	Governing Equations	Variables
Trade winds (planetary / intraseasonal)	$\frac{DU}{DT} - \hat{f}V = -P_X - \hat{d}(U - U_0)$ $\hat{f}U = -\varepsilon^2 \hat{d} V$ $\frac{D\Theta}{DT} + N^2 W = -\hat{d}_\theta \Theta + S_\theta$ $P_z = \Theta$ $U_X + \rho_0^{-1}(\rho_0 W)_z = 0$ $\frac{DQ}{DT} - Q_0 W = -S_\theta$	$\hat{d}, \hat{d}_\theta$ from $\mathcal{O}(\varepsilon)$ $\frac{D}{DT} = \frac{\partial}{\partial T} + U\frac{\partial}{\partial X} + W\frac{\partial}{\partial z}$ U, P, Θ, Q from $\mathcal{O}(1)$ V, W, S_θ from $\mathcal{O}(\varepsilon)$
Planetary / intraseasonal anomalies from the climatology	$\frac{Du}{DT} + uU_X + wU_z - \hat{f}v = -p_X - \hat{d}u$ $\quad -\rho_0^{-1}\left(\rho_0 \langle \overline{w^* u^*} \rangle^p\right)_z - \rho_0^{-1}\left(\rho_0 \langle \overline{w' u'} \rangle^p\right)_z$ $\hat{f}u = -\varepsilon^2 \hat{d} v$ $\frac{D\theta}{DT} + u\Theta_X + w\Theta_z + N^2 w = -\hat{d}_\theta \theta + s_\theta$ $\quad -\rho_0^{-1}\left(\rho_0 \langle \overline{w^* \theta^*} \rangle^p\right)_z - \rho_0^{-1}\left(\rho_0 \langle \overline{w' \theta'} \rangle^p\right)_z$ $p_z = \theta$ $u_X + \rho_0^{-1}(\rho_0 w)_z = 0$ $\frac{Dq}{DT} + uQ_X + wQ_z - Q_0 w = -s_\theta$ $\quad -\rho_0^{-1}\left(\rho_0 \langle \overline{w^* q^*} \rangle^p\right)_z - \rho_0^{-1}\left(\rho_0 \langle \overline{w' q'} \rangle^p\right)_z$	$N^2 = 1$ u, p, θ, q from $\mathcal{O}(\varepsilon)$ v, w, s_θ from $\mathcal{O}(\varepsilon^2)$
Synoptic fluctuations in space or time	$u^*_t + Uu^*_x + w^* U_z - \hat{f}v^* = -p^*_x - \rho_0^{-1}\left(\rho_0 \langle \overline{w' u'} \rangle^s\right)_z$ $v^*_t + Uv^*_x + \hat{f}u^* = -\rho_0^{-1}\left(\rho_0 \langle \overline{w' v'} \rangle^s\right)_z$ $\theta^*_t + U\theta^*_x + w^*\Theta_z + N^2 w^* = -\rho_0^{-1}\left(\rho_0 \langle \overline{w' \theta'} \rangle^s\right)_z + s^*_\theta$ $p^*_z = \theta^*$ $u^*_x + \rho_0^{-1}(\rho_0 w^*)_z = 0$ $q^*_t + Uq^*_x + w^* Q_z - Q_0 w^* = -s^*_\theta - \rho_0^{-1}\left(\rho_0 \langle \overline{w' q'} \rangle^s\right)_z$	all variables from $\mathcal{O}(\varepsilon)$
Mesoscale fluctuations in space and time	$u'_\tau + Uu'_{x'} + w' U_z = -p'_{x'}$ $v'_\tau + Uv'_{x'} = 0$ $\theta'_\tau + U\theta'_{x'} + w'\Theta_z + N^2 w' = s'_\theta$ $p'_z = \theta'$ $u'_{x'} + \rho_0^{-1}(\rho_0 w')_z = 0$ $q'_\tau + Uq'_{x'} + w' Q_z - Q_0 w' = -s'_\theta$	u', v', p', θ', q' from $\mathcal{O}(\varepsilon)$ w', s'_θ from $\mathcal{O}(1)$

TABLE 4: Multi-scale asymptotic model across planetary-, synoptic- and meso-scales in the strong rotation regime.

Regime 3: Strong Rotation ($\hat{f}$ from $\mathscr{O}\left(\varepsilon^{-1}\right)$)		
Space and Time Scales	Governing Equations	Variables
Planetary / synoptic-time circulation	$U_t - \hat{f}V = -P_X - \hat{d}\,(U - U_0)$ $\hat{f}U = -\varepsilon^2 \hat{d}V$ $\Theta_t + N^2 W = S_\theta - \hat{d}_\theta \Theta$ $P_z = \Theta$ $U_X + \rho_0^{-1}\,(\rho_0 W)_z = 0$	$\hat{d}, \hat{d}_\theta$ from $\mathscr{O}\,(1)$ U, P, Θ, S_θ from $\mathscr{O}\,(1)$ V, W from $\mathscr{O}\,(\varepsilon)$
Synoptic fluctuations in QG regime	$\frac{D}{Dt}\left(\phi^*_{xx} + \hat{f}^2 \phi^*_{zz}\right) = -\hat{d}\phi^*_{xx} - \hat{d}_\theta \hat{f}^2 \phi^*_{zz} + \hat{f}\left(s^*_\theta\right)_z$	$\frac{D}{Dt} = \frac{\partial}{\partial t} + U\frac{\partial}{\partial x}$ $u^* = 0, v^* = \phi^*_x, \theta^* = \hat{f}\phi^*_z$ all variables from $\mathscr{O}\,(1)$
Mesoscale fluctuations in space and time	$u'_\tau + (U + u^*)\,u'_{x'} + w'\,(U + u^*)_z - \hat{f}v' = -\,(p')_{x'}$ $v'_\tau + (U + u^*)\,v'_{x'} + w' v^*_z + \hat{f}u' = 0$ $N^2 w' = s'_\theta$ $u'_{x'} + \rho_0^{-1}\,(\rho_0 w')_z = 0$	u', v' from $\mathscr{O}\,(\varepsilon)$ w' from $\mathscr{O}\,(1)$ p' from $\mathscr{O}\left(\varepsilon^2\right)$ s'_θ from $\mathscr{O}\left(\varepsilon^{-1}\right)$

LIST OF FIGURES

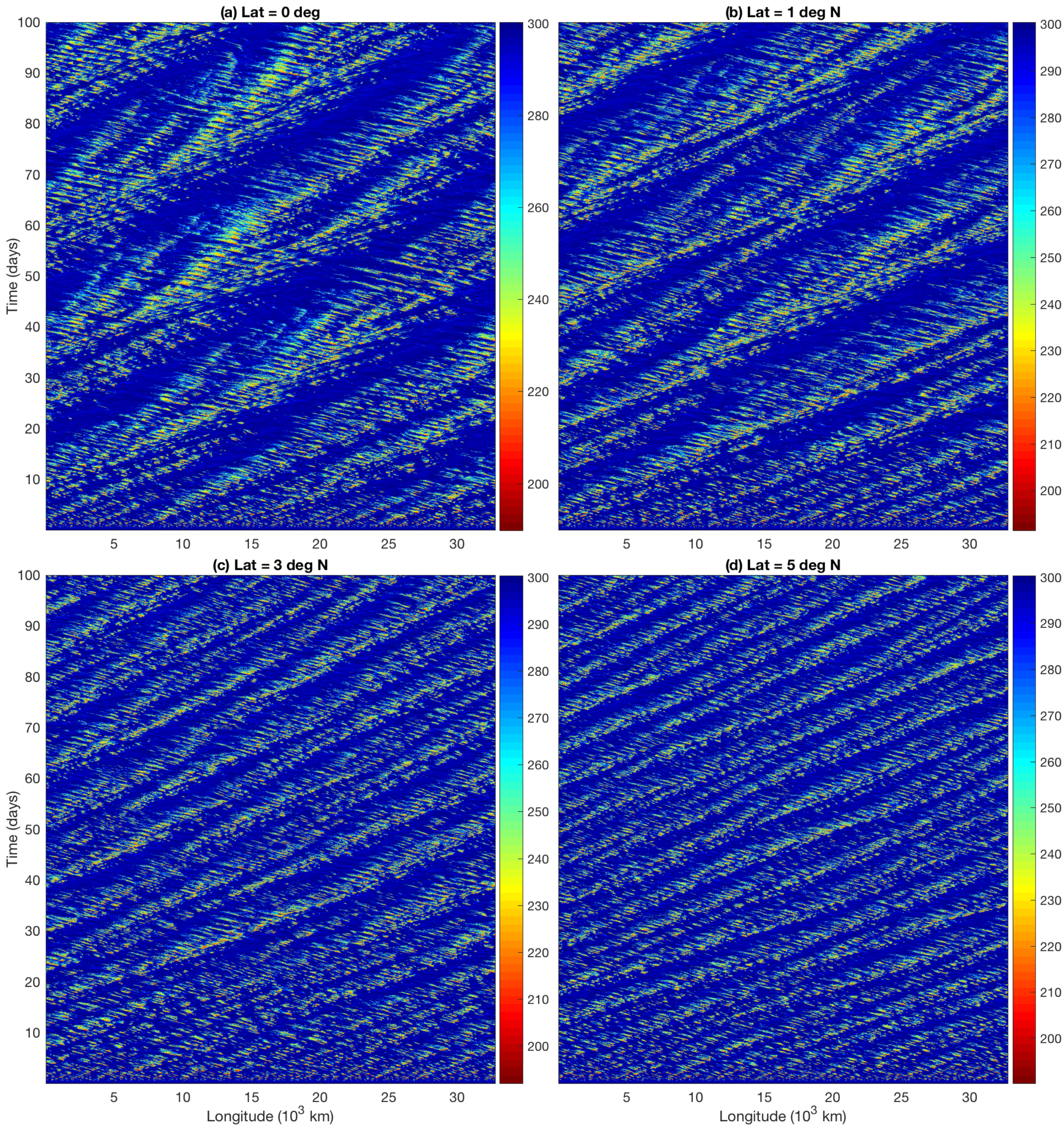

FIG. 1: Hovmöller diagrams of brightness temperature in cases with various magnitude of rotation. These panels correspond to the cases with f at the latitude (a) 0 deg, (b) 1 deg N, (c) 3 deg N, (d) 5 deg N, (e) 9 deg N, (f) 14 deg N, (g) 20 deg N, (h) 27 deg N. Depending on the magnitude of rotation, panels a-d, e-g, and h belong to the weak, order-one, and strong rotation regime, respectively. The output is coarse-grained into 16-km grid resolutions (averaged over every 8 x-grids). The unit is K.

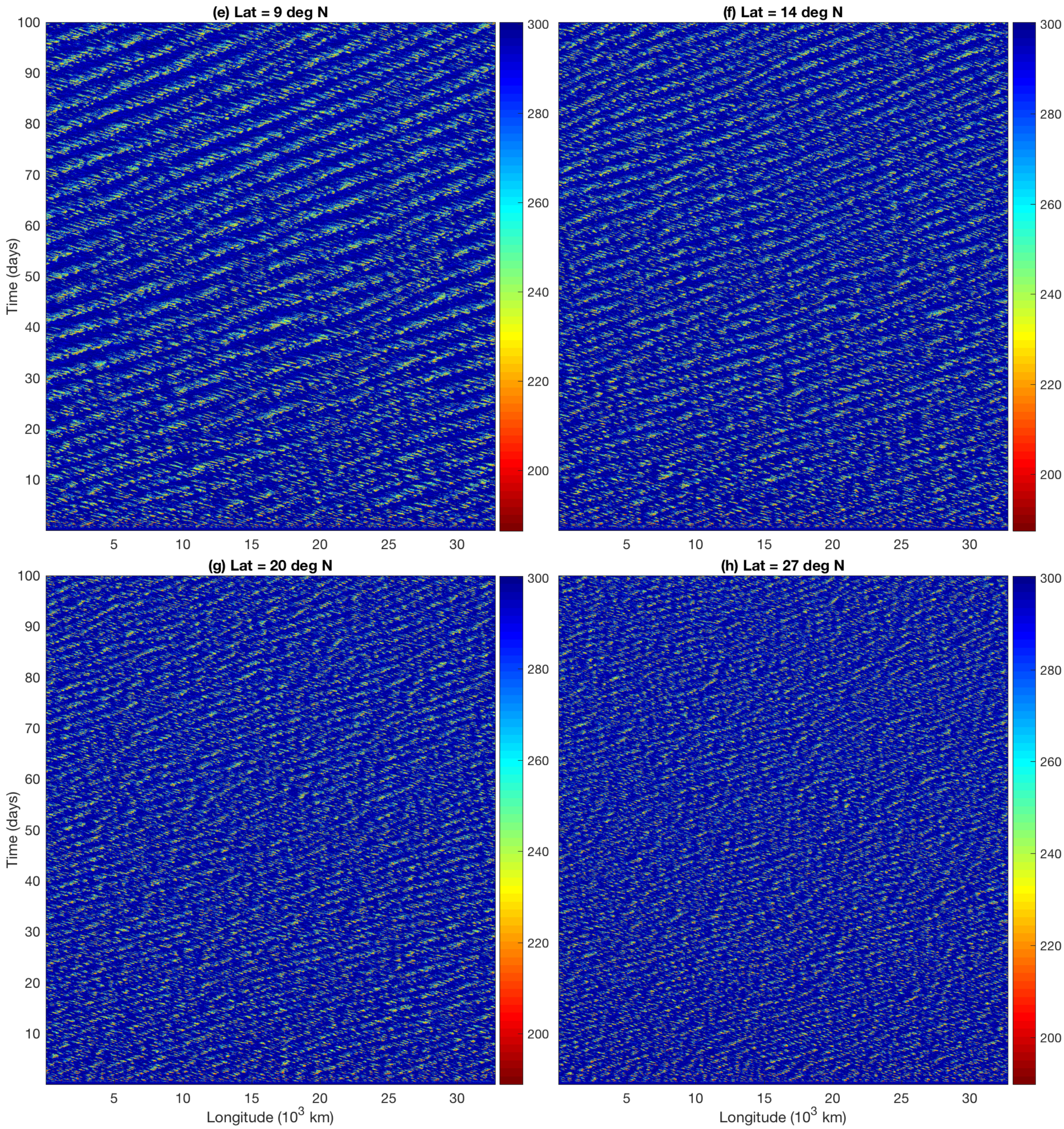

Fig. 1 continued.

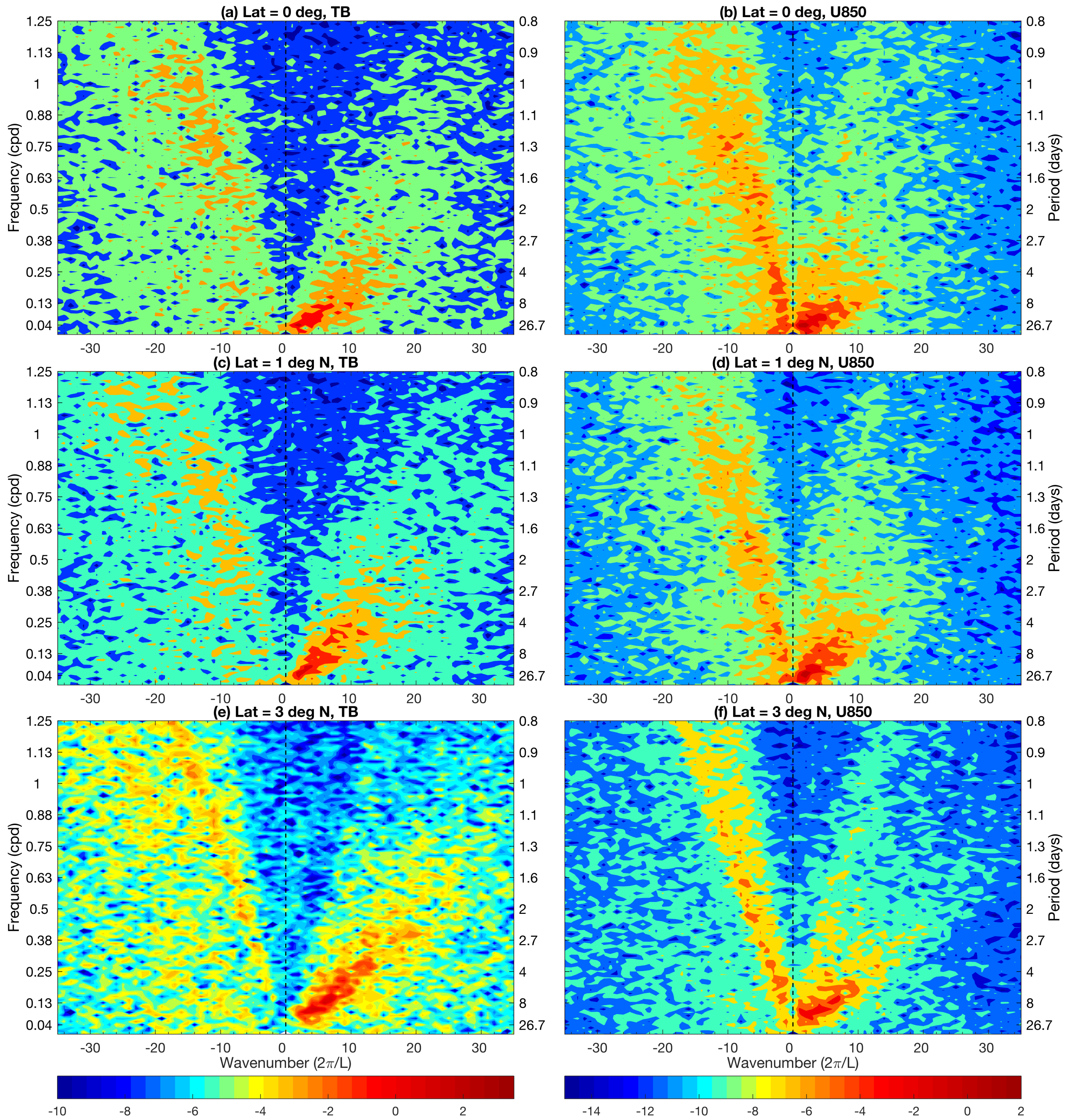

FIG. 2: Log-scale wavenumber-frequency spectra of brightness temperature (left) and 850-hPa zonal velocity (right) in cases with various magnitude of rotation based on the last 80-day output. These panels correspond the cases with f at the latitude (a,b) 0 deg, (c,d) 1 deg N, (e,f) 3 deg N, (g,h) 5 deg N, (i,j) 9 deg N, (k,l) 14 deg N, (m,n) 20 deg N, (o,p) 27 deg N, (q,r) 35 deg N. The value at the origin (zonal and time mean) is removed. The dimensional units of brightness temperature and zonal velocity is K and m/s, respectively.

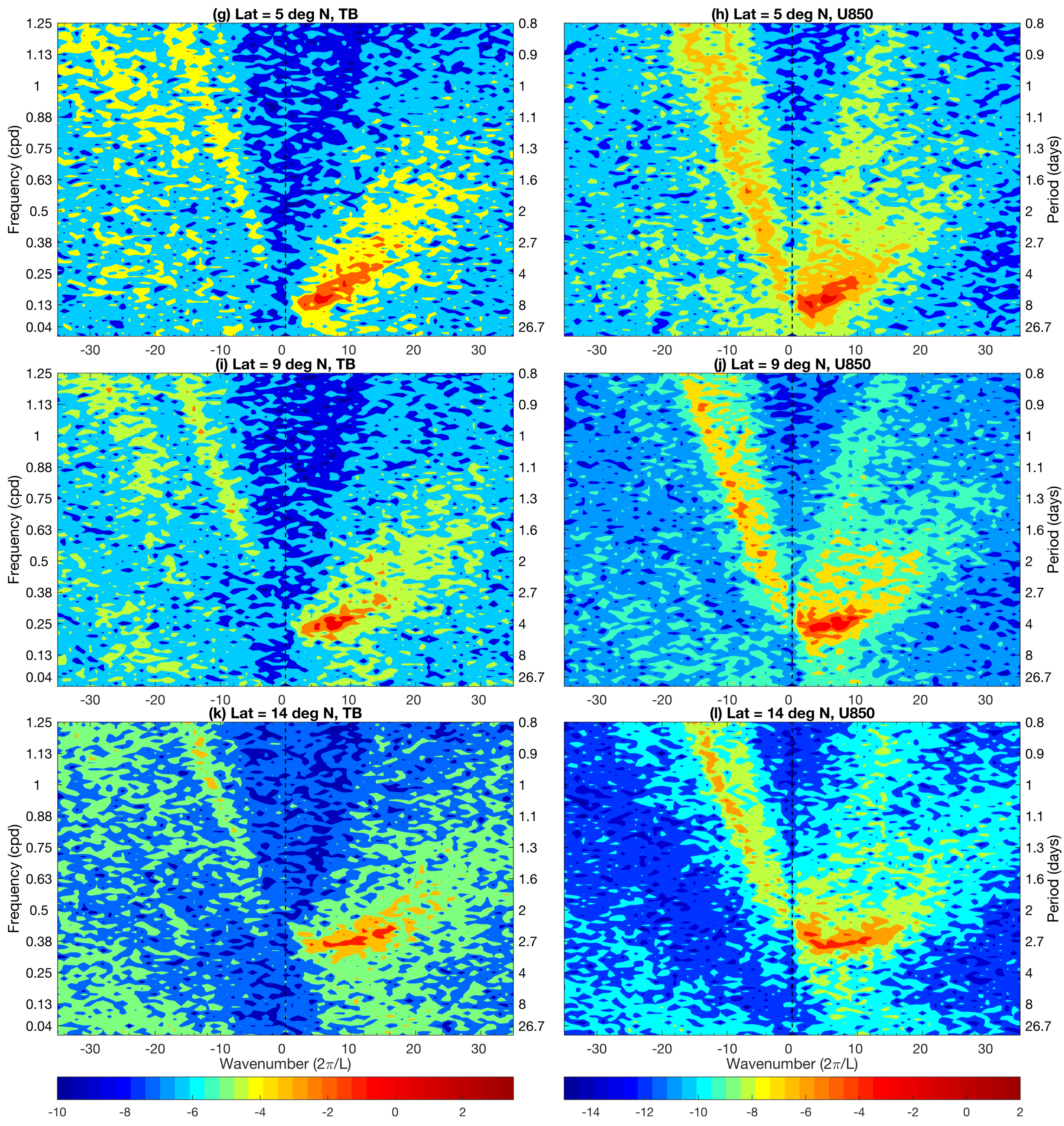

Fig. 2 continued.

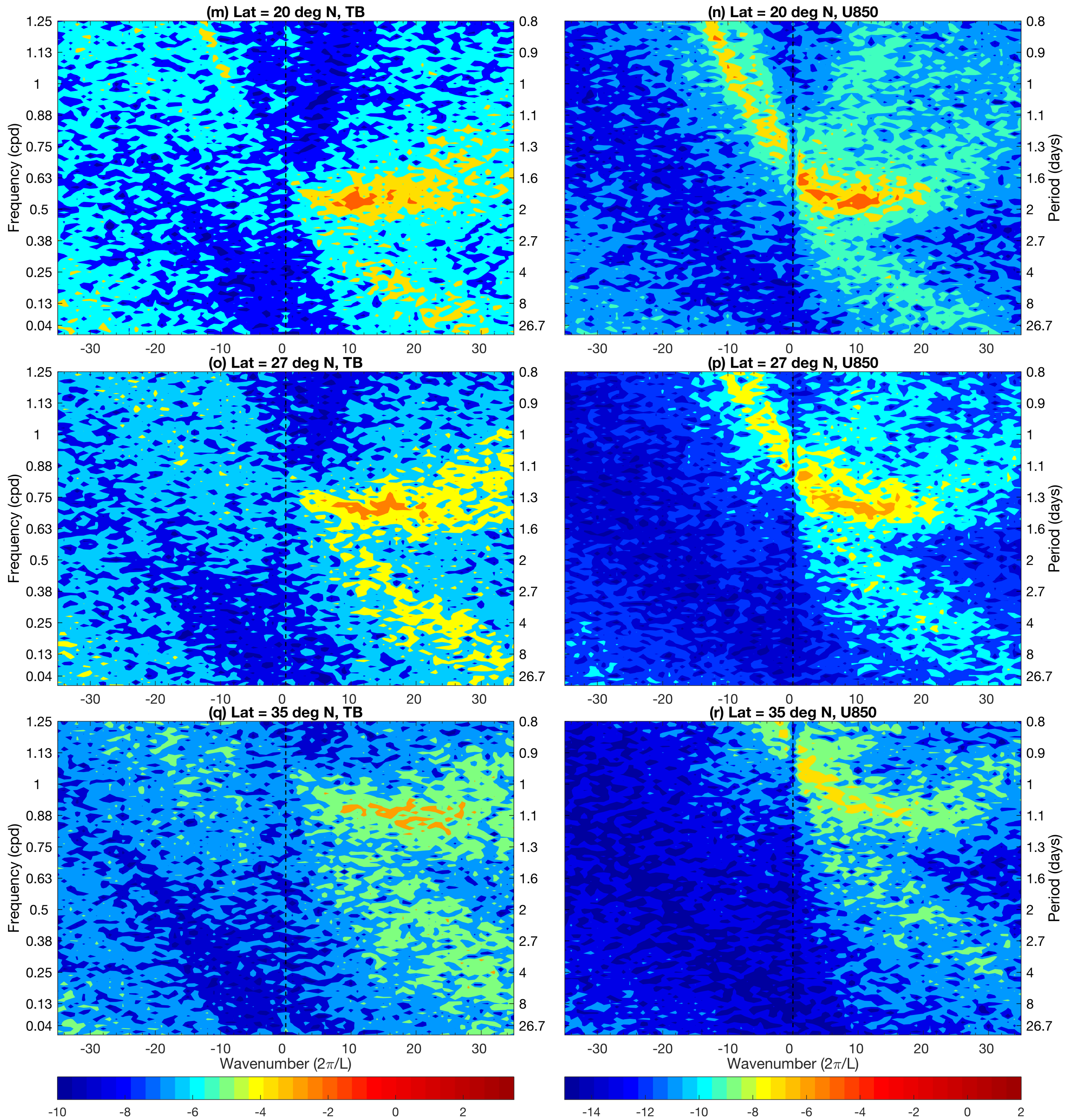

Figure 2 continued.

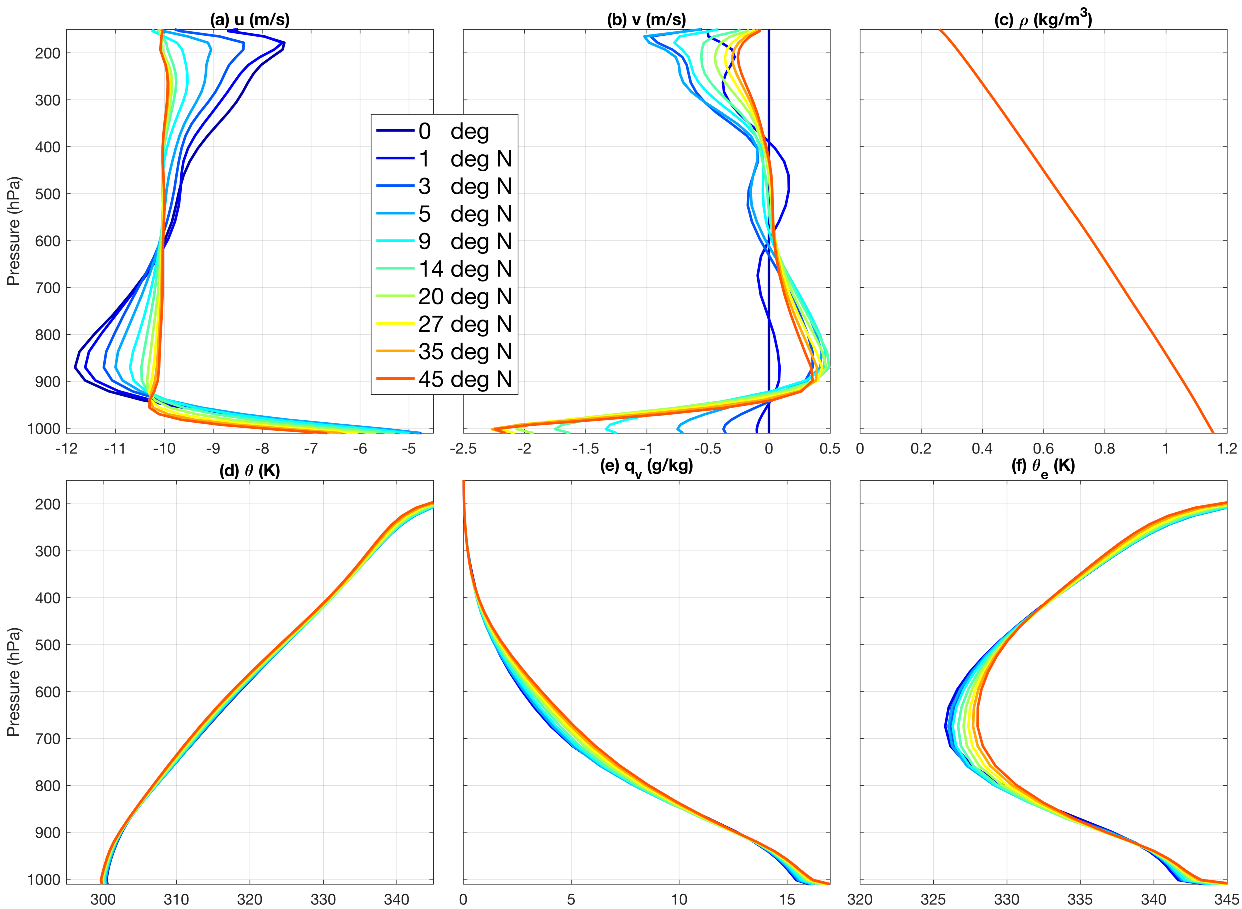

FIG. 3: Domain-mean climatology of (a) zonal velocity, (b) meridional velocity, (c), air density, (d) potential temperature, (e) water vapor, (f) equivalent potential temperature in these 10 cases based on last 80-day output. The horizontal axis shows the value of each field with its dimensional unit attached in the subtitle.

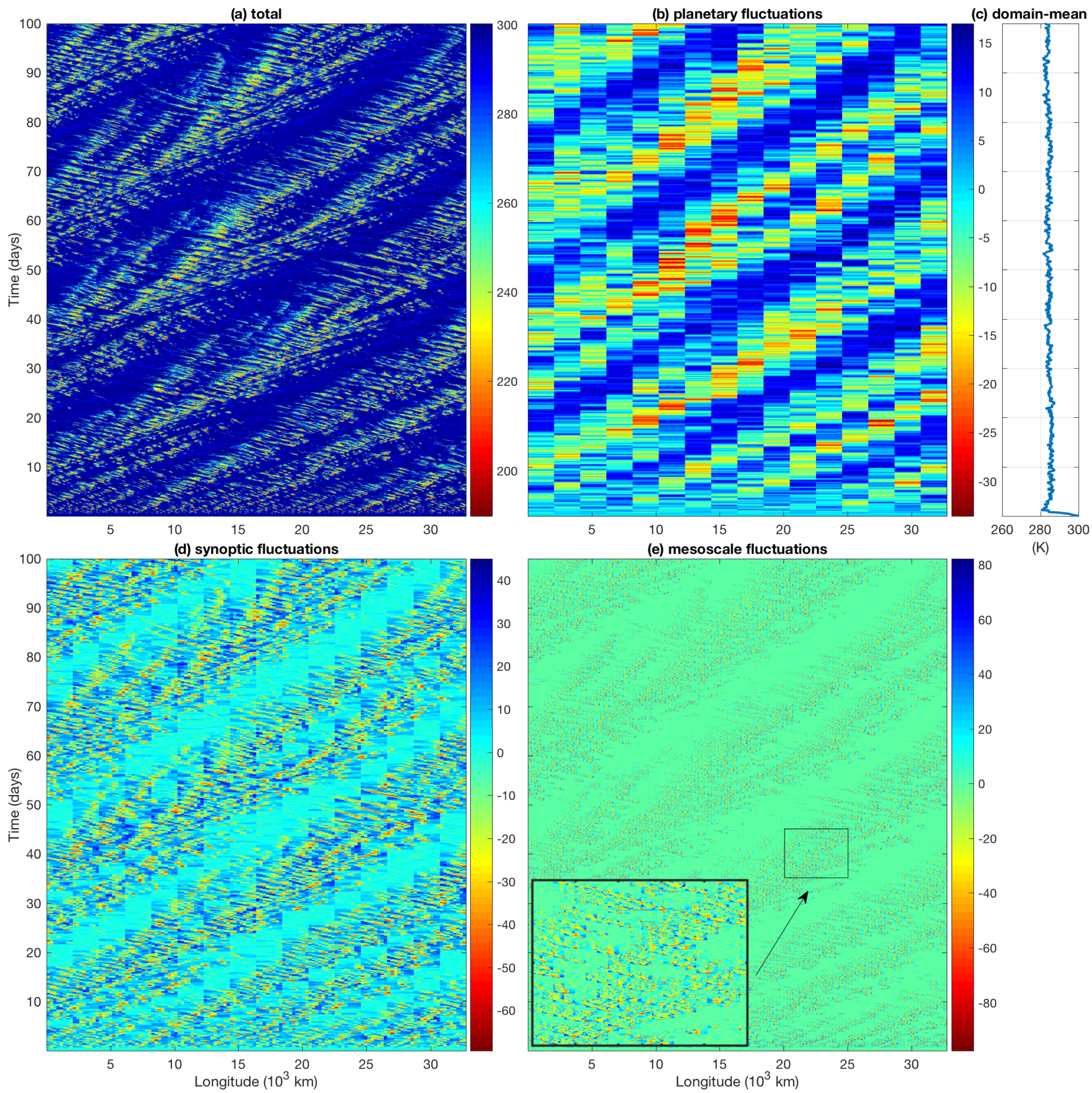

FIG. 4: Multi-scale decomposition of brightness temperature field in the non-rotating case through coarse graining method. Panel (a) shows the total field. Panels (b-d) show (b) planetary fluctuations, (c) domain-mean, (d) synoptic fluctuations, (e) mesoscale fluctuations. Coarse grid size in these panels is (a) 16 km, (b) 2048 km, (d) 256 km, (e) 16 km. The unit is K.

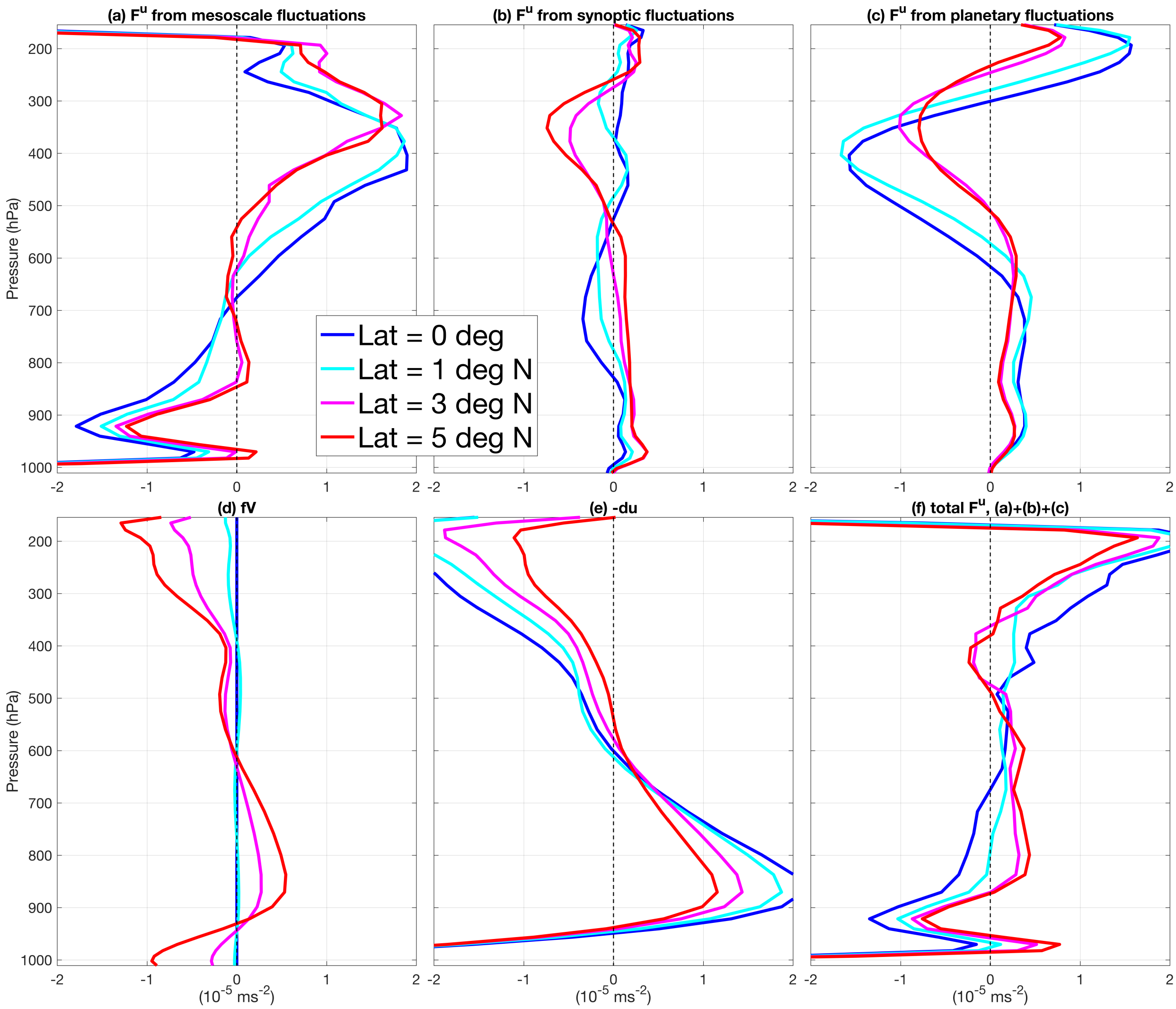

FIG. 5: Vertical profiles of climatological-mean (domain-mean and time-mean) zonal momentum budget terms based on the last 80-day model output in the weak rotation regime. Panels (a-c) show eddy zonal momentum transfer from (a) mesoscale fluctuations, (b) synoptic fluctuations, (c) planetary fluctuations, and panel (f) shows total. The remaining panels show (d) the Coriolis term, and (e) momentum damping. The unit of eddy zonal momentum transfer is ms^{-2}.

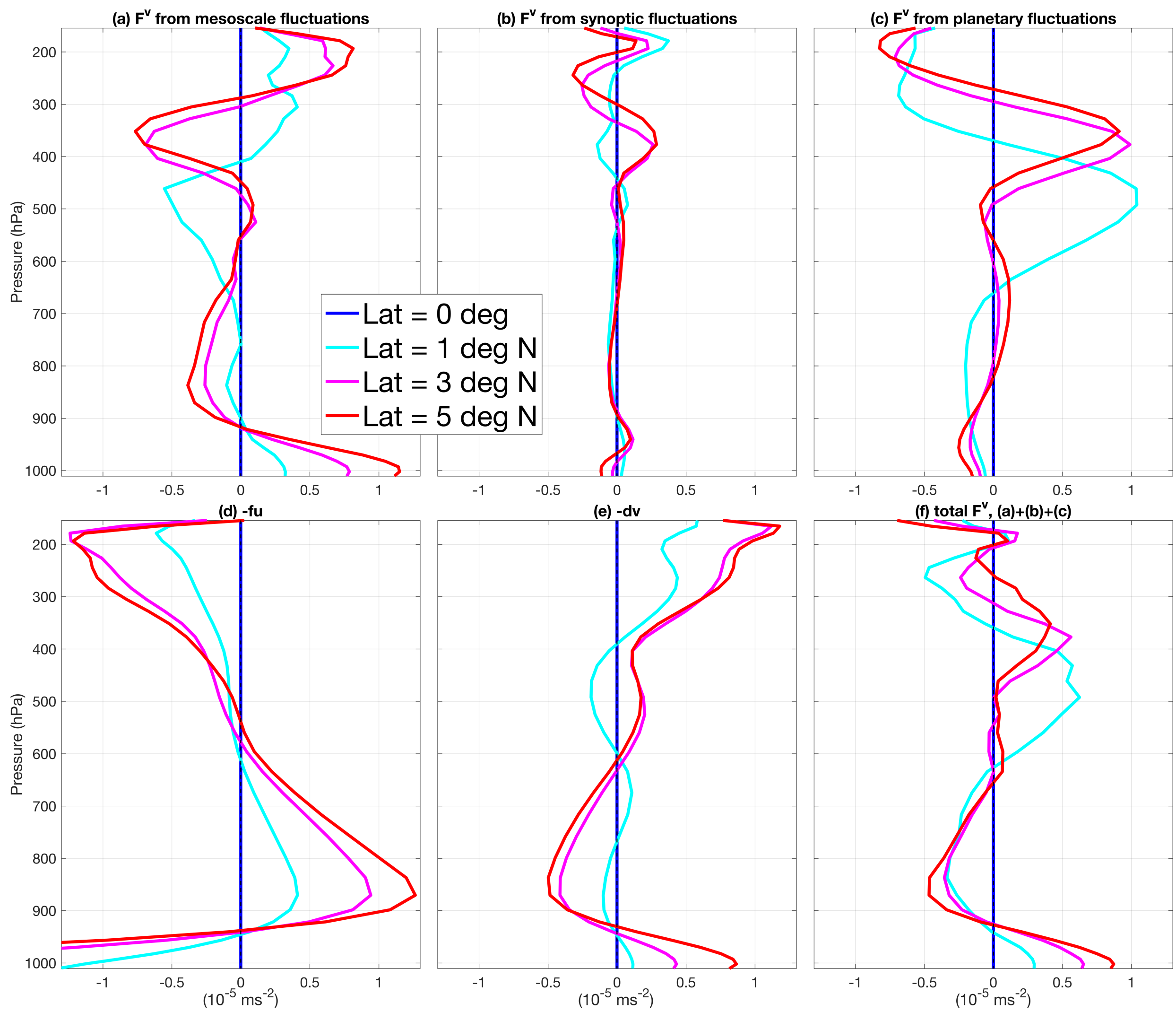

FIG. 6: Vertical profiles of climatological-mean (domain-mean and time-mean) meridional momentum budget terms based on the last 80-day model output in the weak rotation regime. Panels (a-c) show eddy meridional momentum transfer from (a) mesoscale fluctuations, (b) synoptic fluctuations, (c) planetary fluctuations, and panel (f) shows total. The remaining panels show (d) the Coriolis term, and (e) momentum damping. The unit of eddy meridional momentum transfer is ms^{-2}.

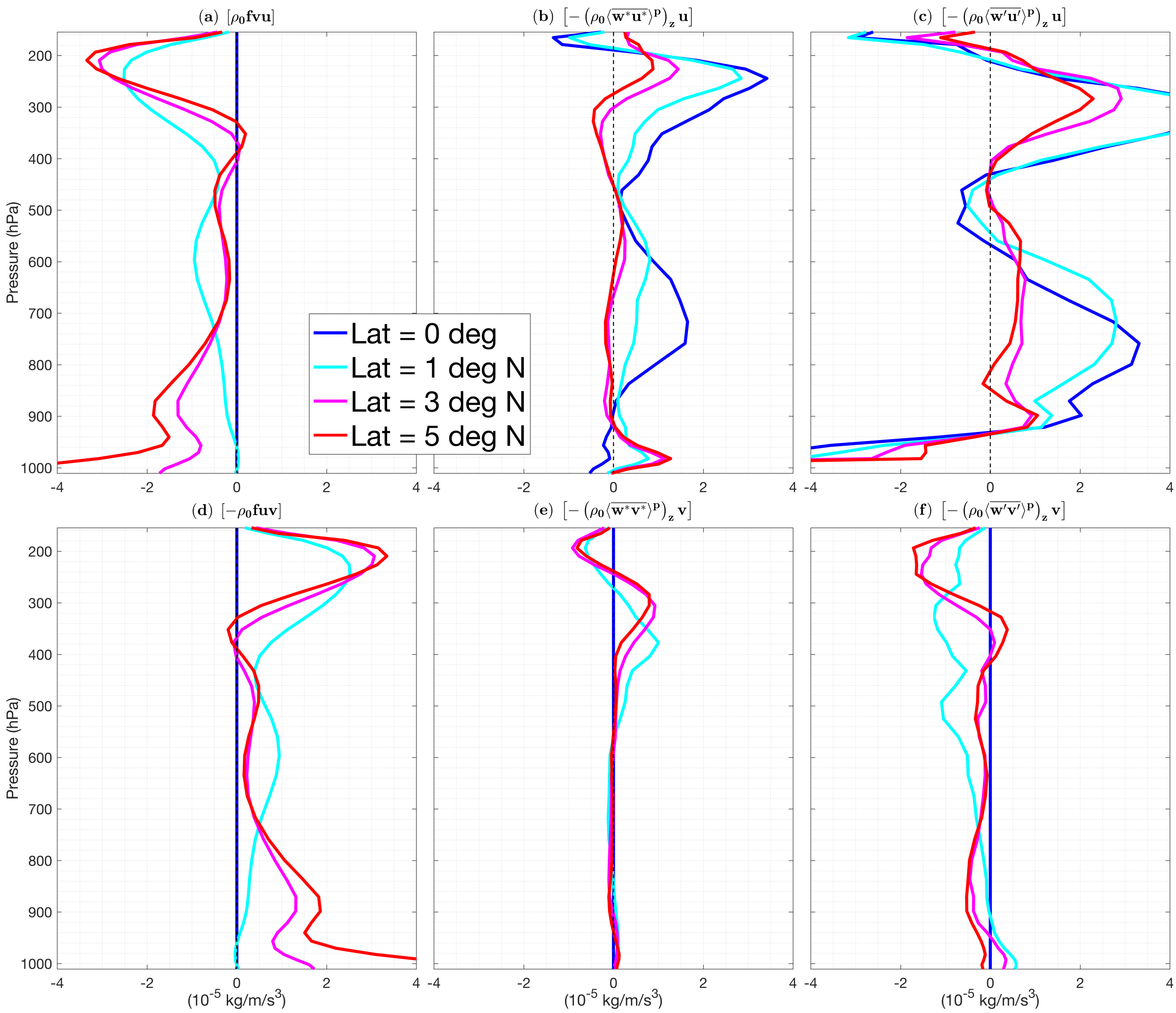

FIG. 7: Vertical profiles of climatological-mean (domain-mean and time-mean) planetary-scale kinetic energy source and sink terms, based on the last 80-day model output in the weak rotation regime. Panels (a-c) show the terms involving (a) the Coriolis force, (b) eddy zonal momentum transfer from synoptic fluctuations, (c) eddy zonal momentum transfer from mesoscale fluctuations. Panels (d-f) are similar to panels (a-c) but for meridional winds. The dimensional unit of all terms is $kgm^{-1}s^{-3}$.

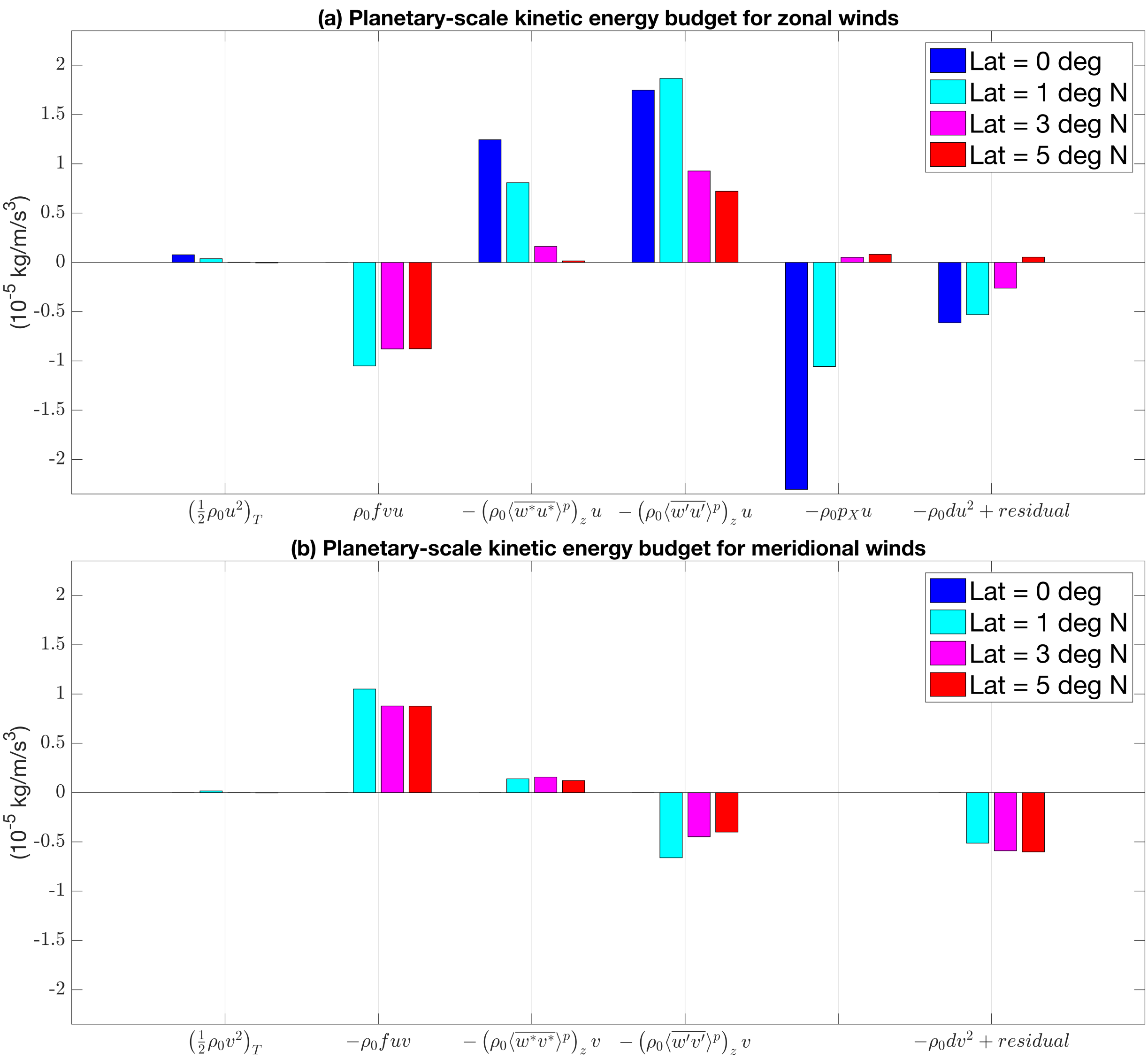

FIG. 8: Climatological-mean (zonal and vertical mean, and time-mean) total planetary-scale kinetic energy source and sink terms for (a) zonal winds, (b) meridional winds, based on the last 80-day model output in the weak rotation regime. The dimensional unit of all terms is $kgm^{-1}s^{-3}$. The y-axis limit in both panels are $2.35 \times 10^{-5} kg/m/s^3$.

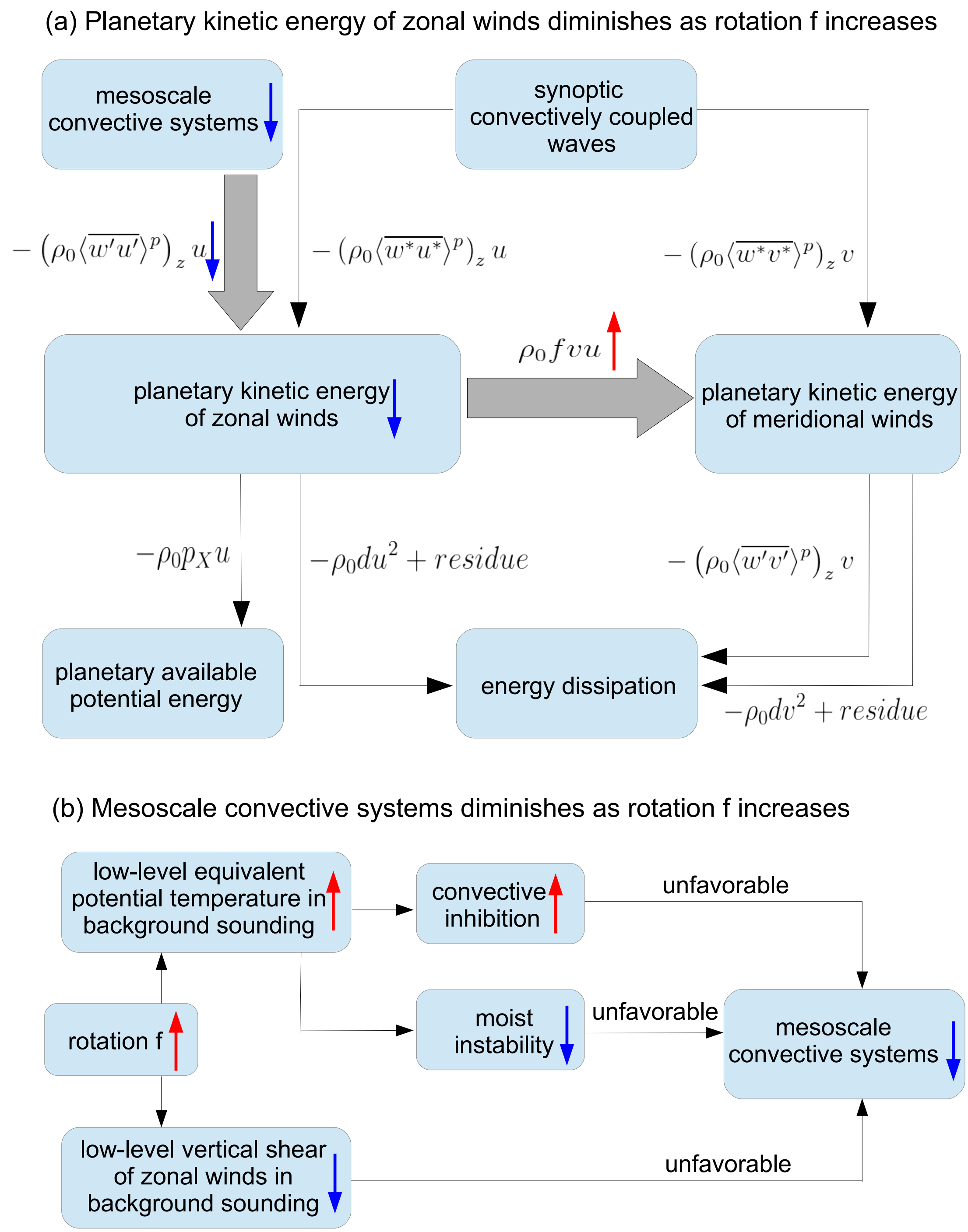

FIG. 9: Schematic diagram explaining why planetary-scale kinetic energy of zonal winds diminishes as the rotation f increases in the weak rotation regime. Panel (a) shows acceleration/deceleration effects in the planetary-scale kinetic energy budget of both zonal and meridional winds, where bold (thin) arrows indicate the dominant (secondary) energy source/sink terms. The red up (blue down) arrow represents increasing (decreasing) in magnitude. Overall, the diminishment of planetary kinetic energy of zonal winds is due to i) increasing deceleration term involving the Coriolis force, and ii) decreasing acceleration term involving eddy zonal momentum transfer from mesoscale fluctuations. Panel (b) attributes the diminishment of mesoscale convective systems to the increasing low-level equivalent potential temperature and decreasing low-level vertical shear in the background sounding as the rotation f increases.

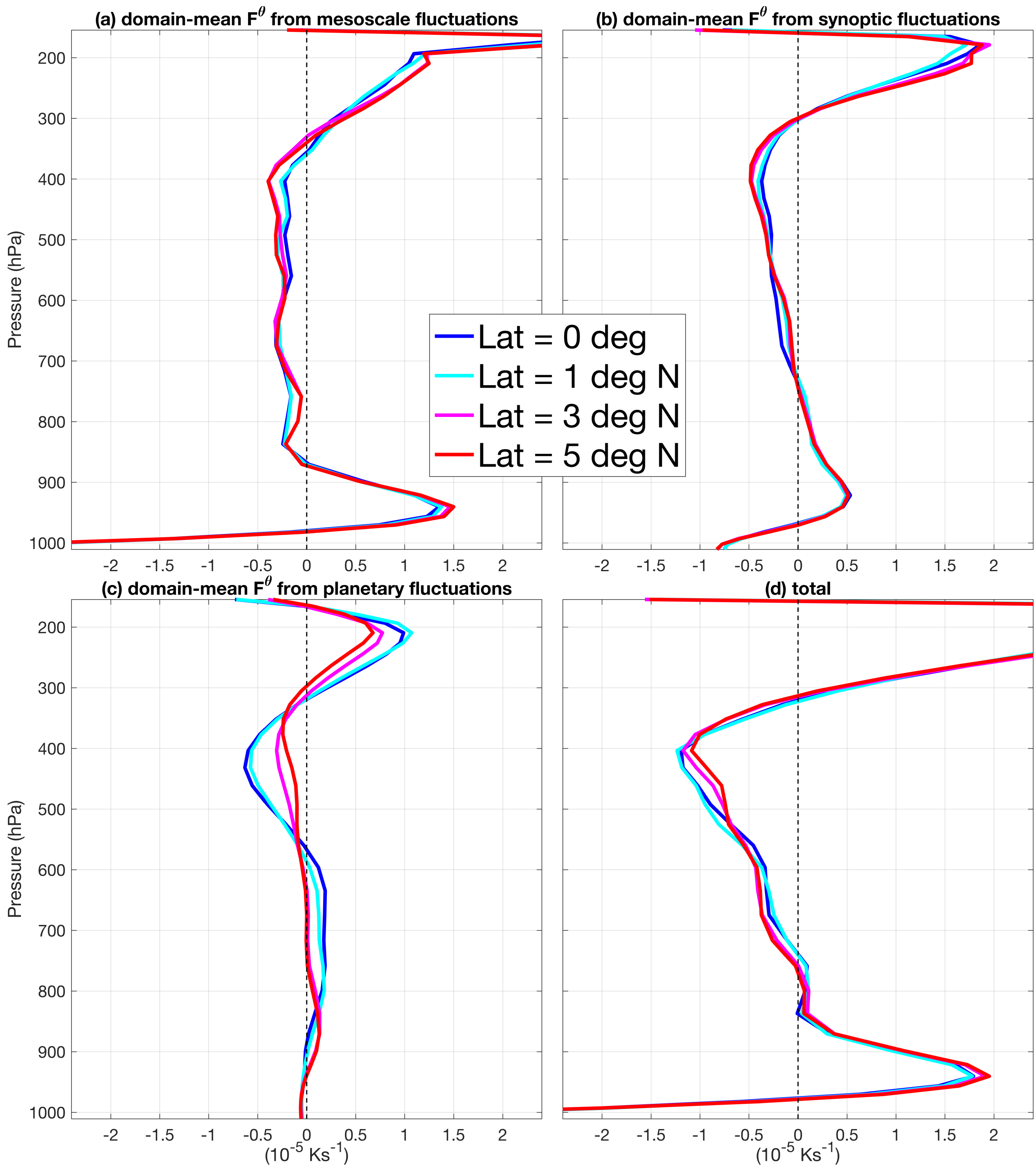

FIG. 10: Vertical profiles of climatological-mean (domain-mean and time-mean) eddy heat transfer from (a) mesoscale fluctuations, (b) synoptic fluctuations, (c) planetary fluctuations, and (d) total, based on the last 80-day model output in the weak rotation regime. The unit of eddy heat transfer is Ks^{-2}.

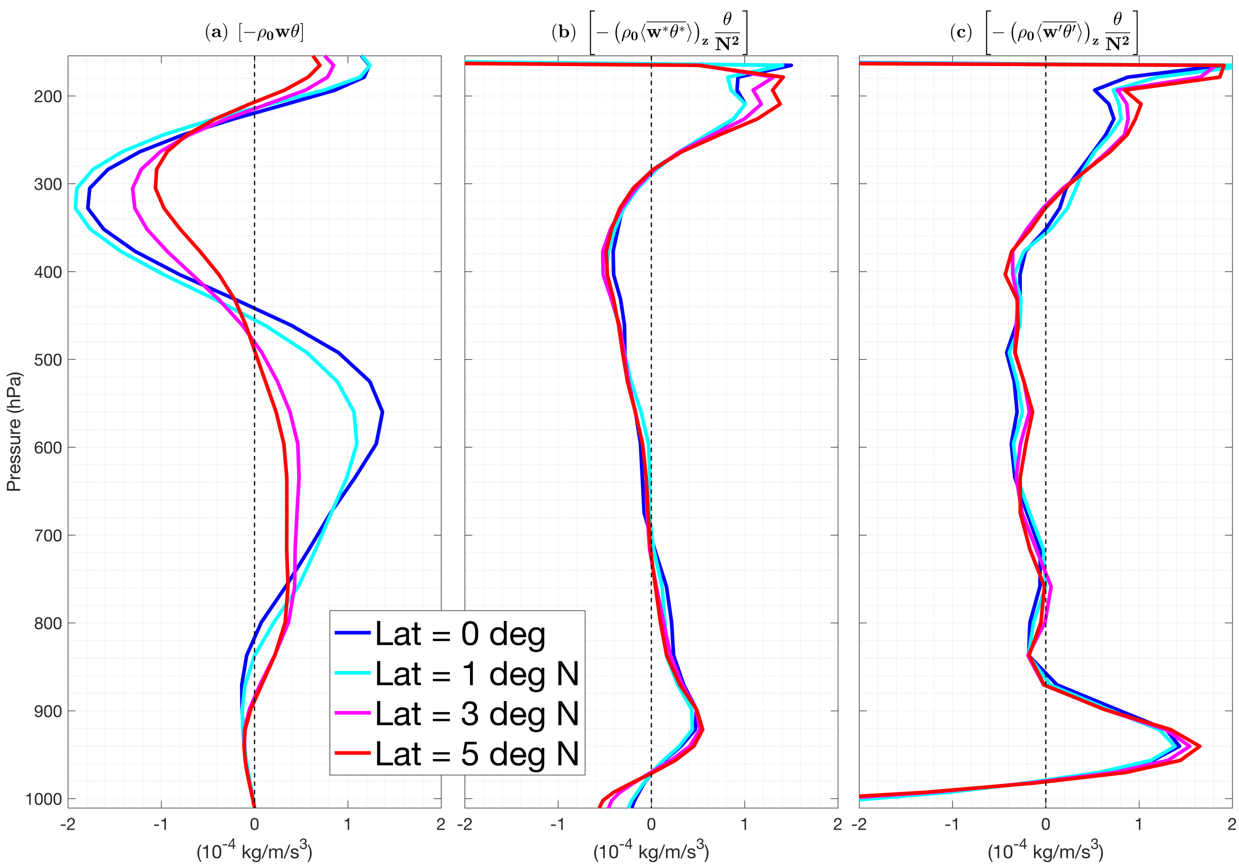

FIG. 11: Vertical profiles of climatological-mean (domain-mean and time-mean) available potential energy source and sink terms, based on the last 80-day model output in the weak rotation regime. Panel (a) shows the term involving energy transfer between kinetic energy and available potential energy. Panels (b-c) show available potential energy source and sinks terms involving eddy heat transfer from (b) synoptic fluctuations, (c) mesoscale fluctuations. Potential temperature is rescaled by a constant, $\tilde{\theta} = \frac{g}{\theta}\theta$. The dimensional unit of all terms is $kgm^{-1}s^{-3}$.

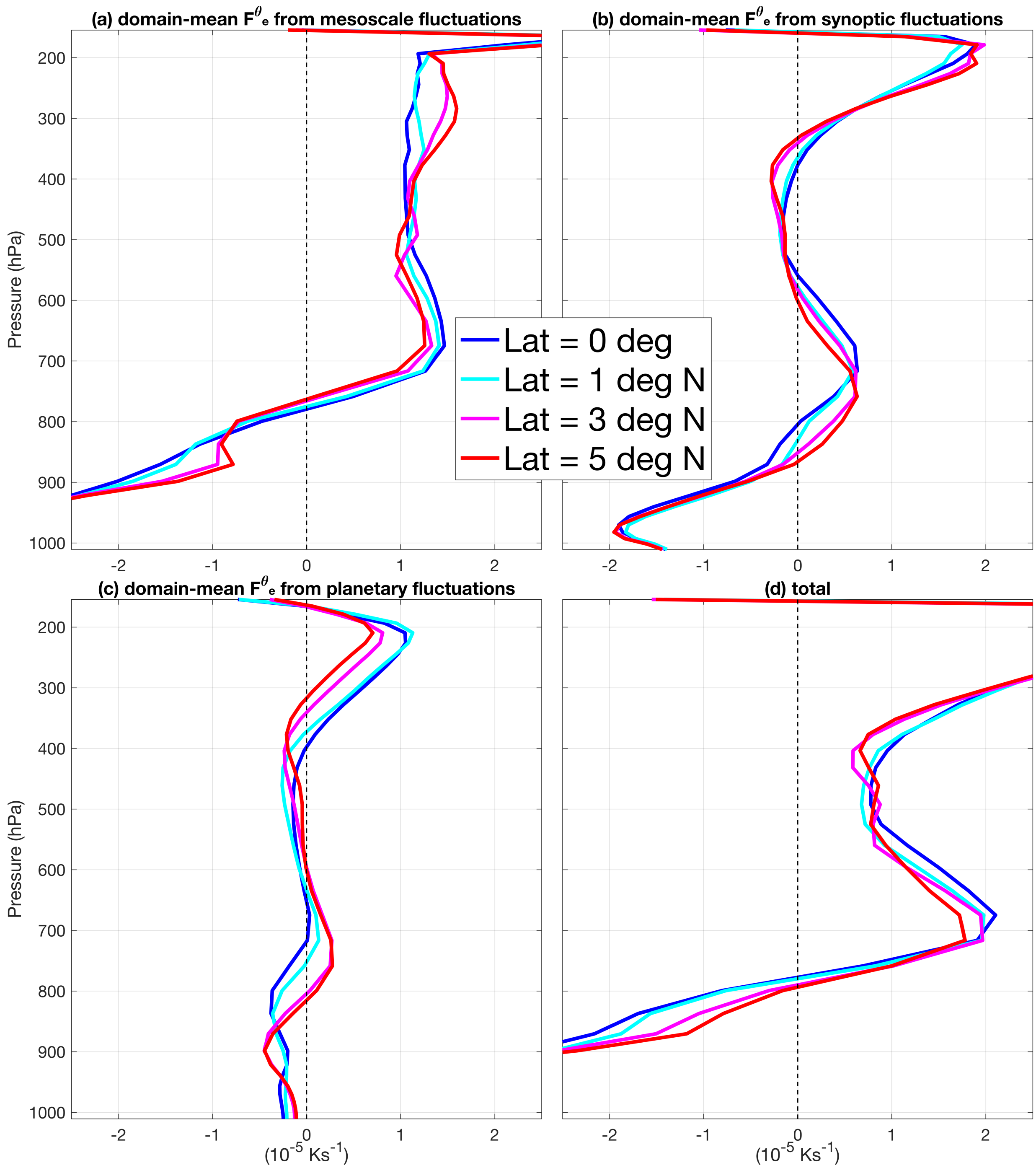

FIG. 12: Vertical profiles of climatological-mean (domain-mean and time-mean) eddy transfer of equivalent potential temperature from (a) mesoscale fluctuations, (b) synoptic fluctuations, (c) planetary fluctuations, and (d) total, based on the last 80-day model output in the weak rotation regime. The unit of eddy transfer of equivalent potential temperature is K/s.

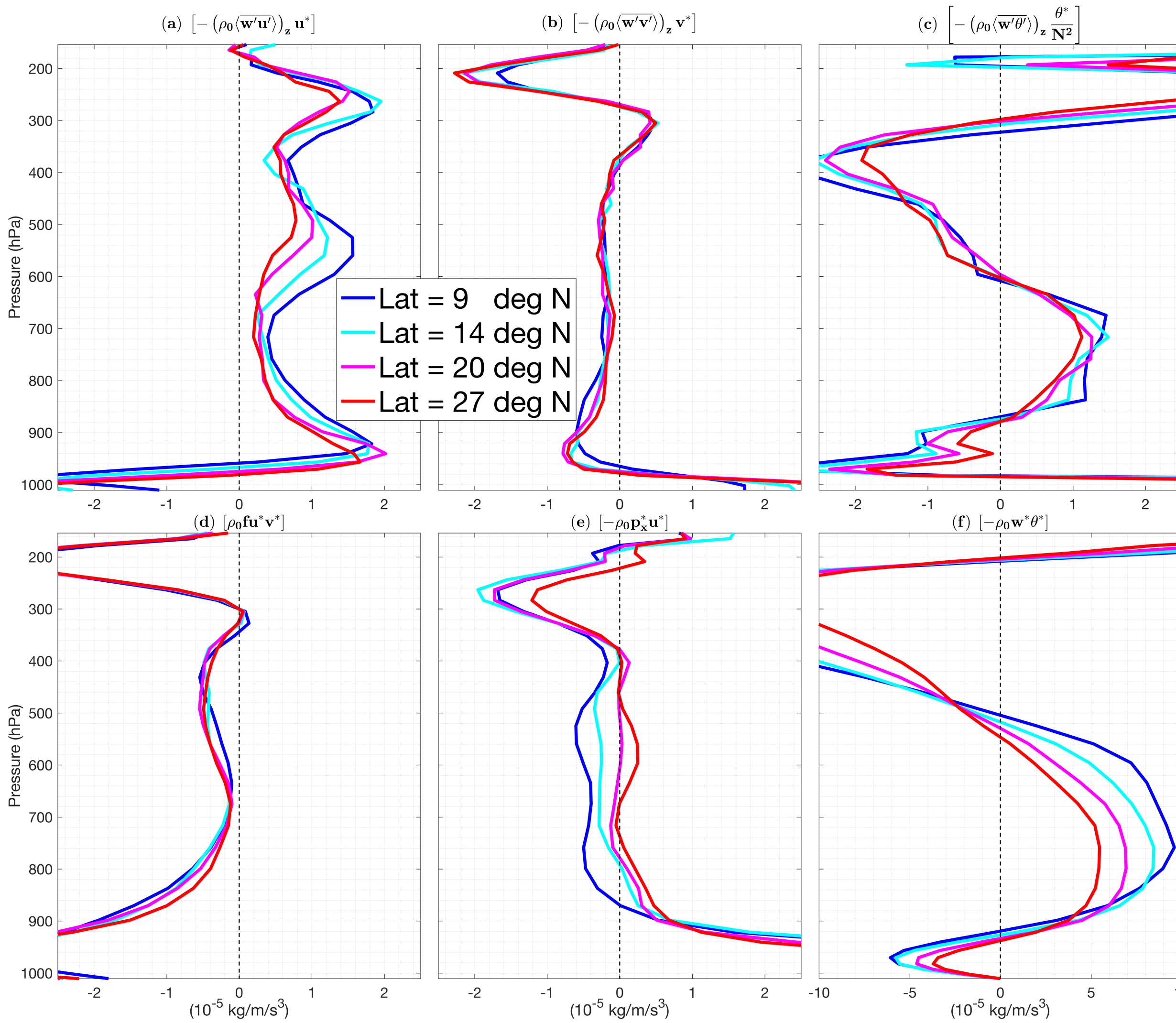

FIG. 13: Vertical profiles of climatological-mean (domain-mean and time-mean) synoptic-scale energy source and sink terms based on the last 80-day model output in the order-one rotation regime. Panels (a-d) show the terms involving (a) eddy zonal momentum transfer, (b) eddy meridional momentum transfer, (c) eddy heat transfer, (d) the Coriolis force. Panel (e-f) show the terms representing energy conversion between kinetic energy and available potential energy. The dimensional unit of all terms is $10^{-5} kgm^{-1}s^{-3}$.

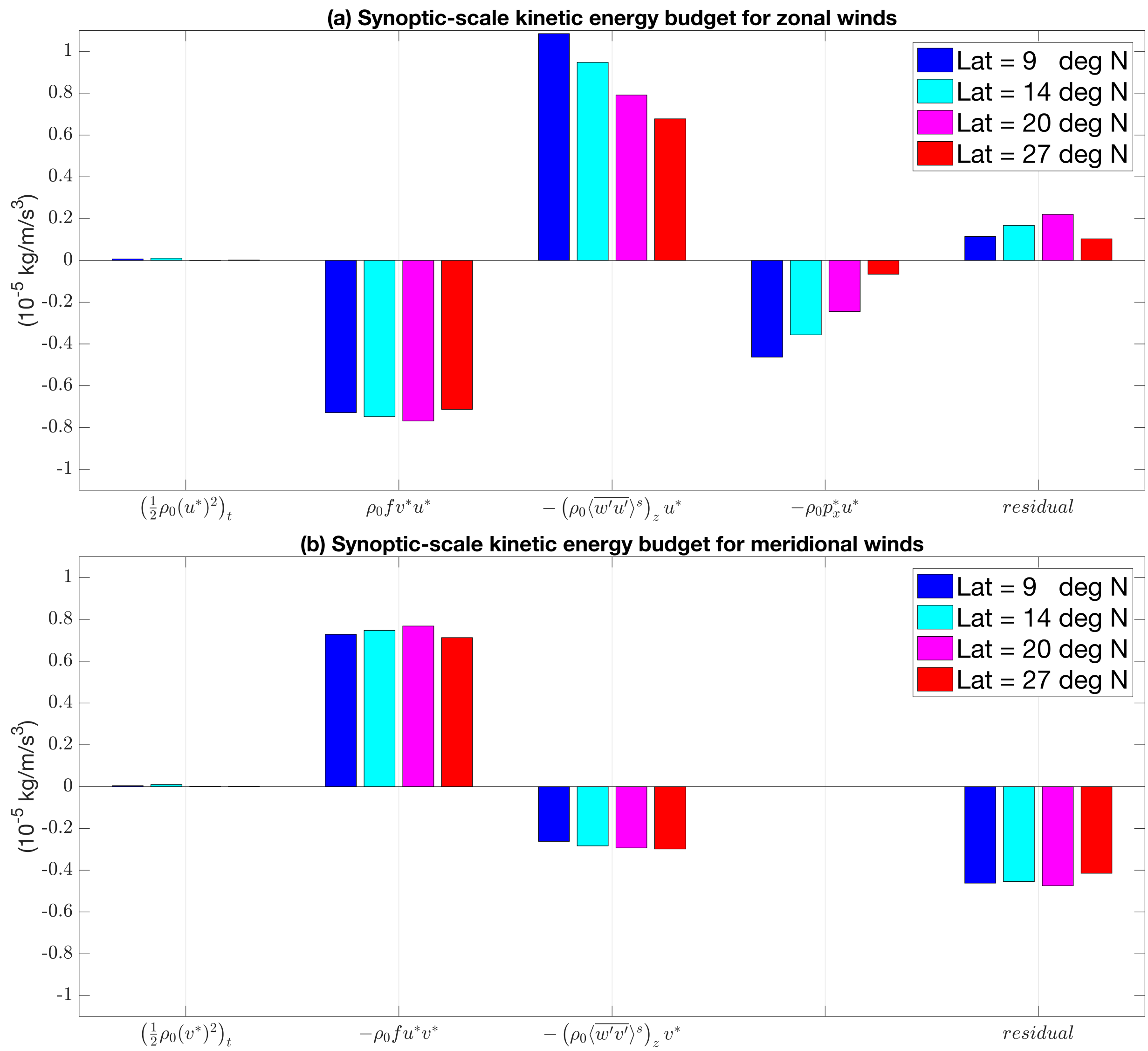

FIG. 14: Climatological-mean (zonal and vertical mean, and time-mean) total synoptic-scale kinetic energy source and sink terms for (a) zonal winds, (b) meridional winds, based on the last 80-day model output in the order-one rotation regime. The dimensional unit of all terms is $kgm^{-1}s^{-3}$. The y-axis limit in both panels are $1.1 \times 10^{-5} kg/m/s^3$.

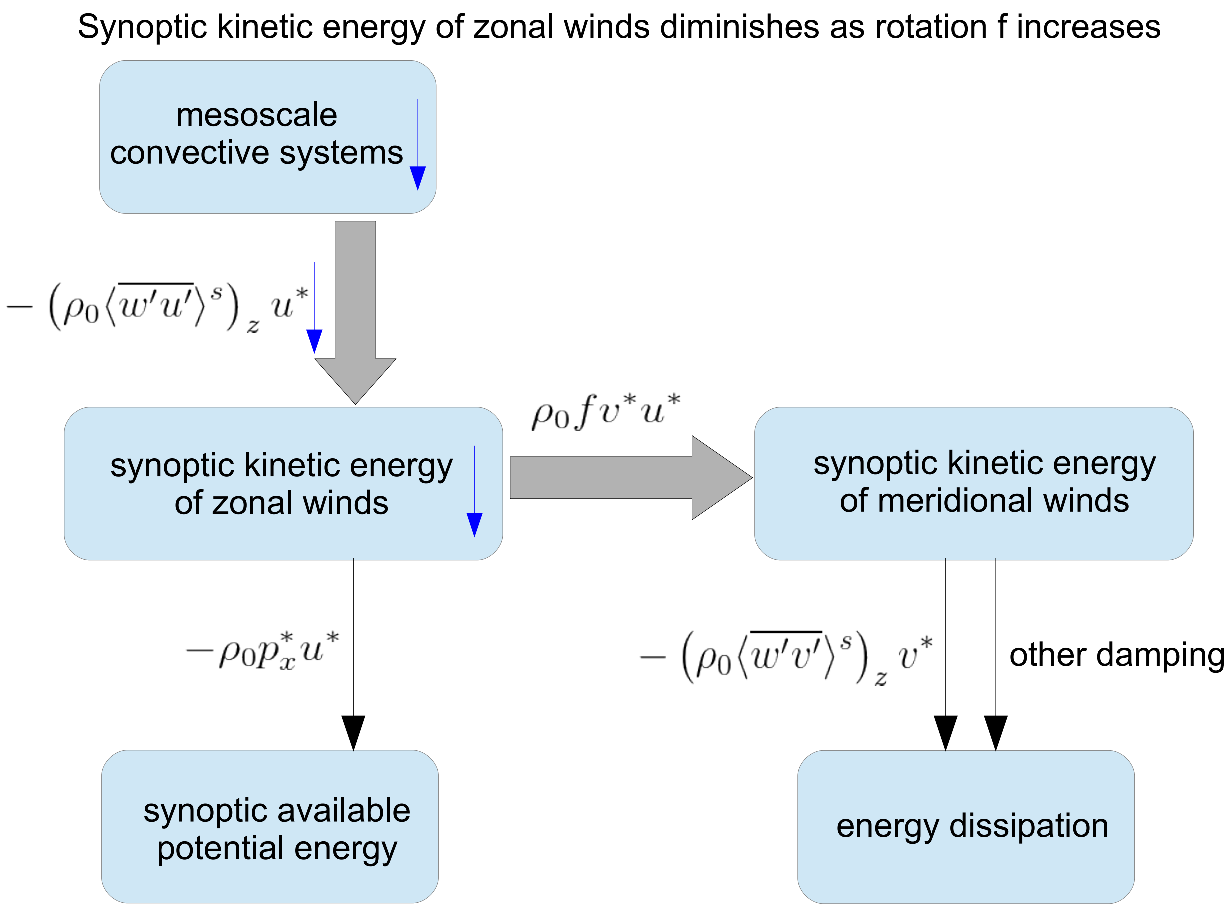

FIG. 15: Schematic diagram explaining the maintenance of synoptic organization of convection and its diminishment as the rotation further increases in the order-one rotation regime. This figure shows acceleration/deceleration effects in the synoptic-scale kinetic energy budget of both zonal and meridional winds, where bold (thin) arrows indicate the dominant (secondary) energy source/sink terms. The blue down arrow represents decreasing in magnitude. Overall, the diminishment of synoptic kinetic energy of zonal winds is due to decreasing acceleration term involving eddy zonal momentum transfer from mesoscale fluctuations. The explanation for the diminishment of mesoscale convective systems is the same as Fig.12, so it is not repeated here.

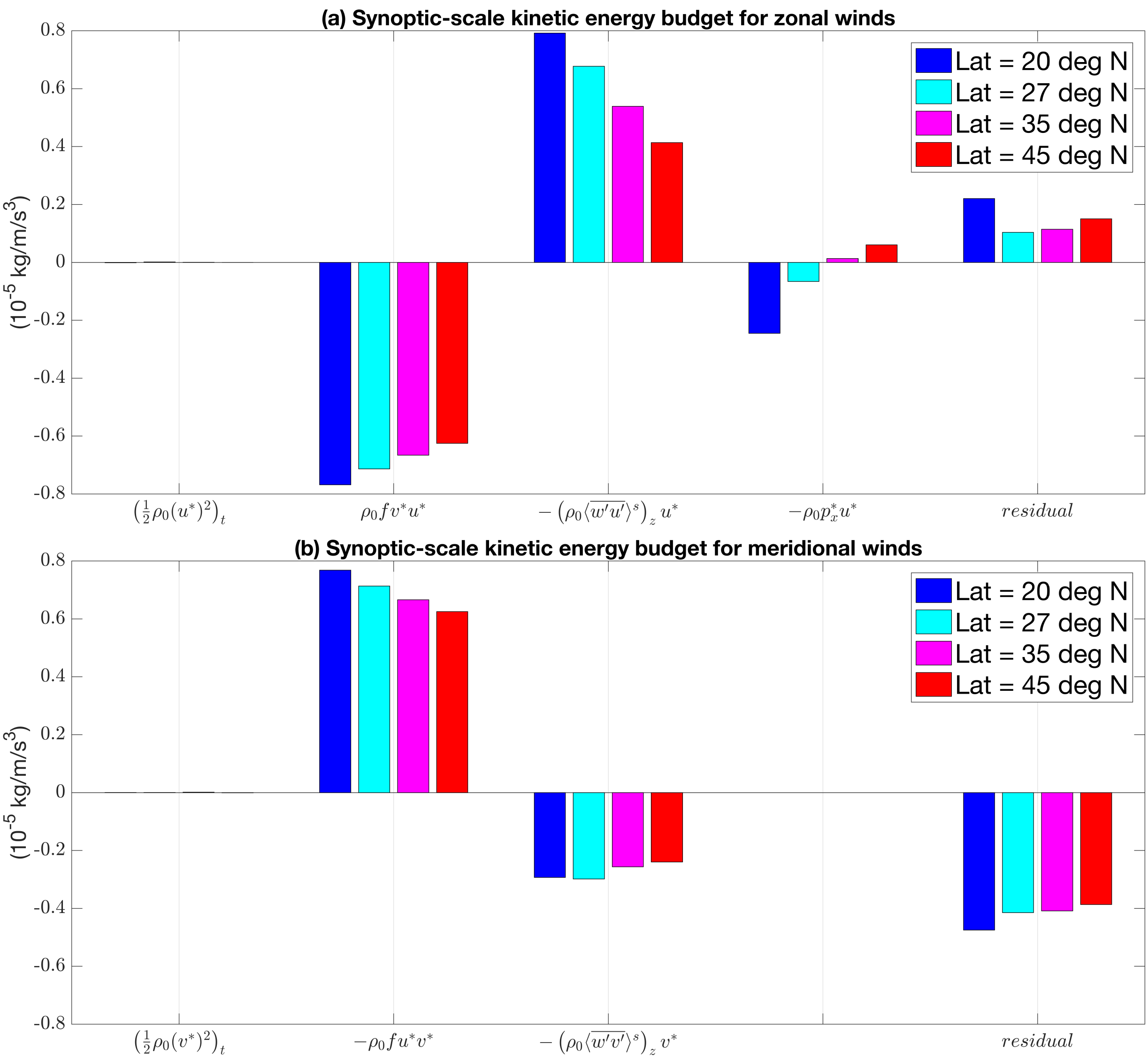

FIG. 16: Climatological-mean (zonal and vertical mean, and time-mean) total synoptic-scale kinetic energy source and sink terms for (a) zonal winds, (b) meridional winds, based on the last 80-day model output in the strong rotation regime. The dimensional unit of all terms is $kgm^{-1}s^{-3}$. The y-axis limit in both panels are $0.80\times 10^{-5}kg/m/s^3$.